Algorithm Theoretical Basis Document (ATBD)

glaciers cci

Prepared by:	Glaciers_cci consortium
Contract:	4000127593/19/I-NB
Name:	Glaciers_cci+D2.1_ATBD
Version:	1.0
Date:	10.10.2020

Contact:
Frank Paul
Department of Geography
University of Zurich
frank.paul@geo.uzh.ch

Technical Officer:
Anna Maria Trofaier
ESA Climate Office

UNIVERSITY OF OSLO   University of Zurich ᵁᶻᴴ   UNIVERSITY OF LEEDS

GAMMA REMOTE SENSING   enveo

Document status sheet

Version	Date	Changes	Approval
0.1	02.04. 2020	Initial draft	
0.2	11.06. 2020	Work-plan from discussion integrated	
0.3	19.06. 2020	Intro for Section 2 and Section 2.1 added	
0.4	28.08. 2020	Integrated and compiled complete document version	A. Kääb
0.5	07.09. 2020	Final version for review	F. Paul
1.0	10.10. 2020	Comments of TO integrated	F. Paul

Author team:
Andreas Kääb, Désirée Treichler (GUIO), Thomas Nagler, Jan Wuite (ENVEO), Tazio Strozzi, Andreas Wiesmann (Gamma), Frank Paul, Philipp Rastner (GIUZ), Lin Gilbert, Andrew Shepherd (SEEL),

Glaciers_cci Technical Officer at ESA:
Anna Maria Trofaier

Related documents

Acronym	Title	Document reference	Version	Date
[RD1]	Algorithm Development Plan	Glaciers_cci+D1.2_ADP	0.1	02.02.2020
[RD2]	Algorithm Theoretical Basis Document	Glaciers_cci_ph2_D21_ATBD_v25	2.5	02.05.2016

Table of Contents

1. Purpose of this document

The document provides a detailed description of algorithms chosen to generate Fundamental Climate Data Records (FCDRs) of the data products requested by the users. Thereby, focus is on new or revised algorithms compared to the Glaciers_cci Phase 2 ATBD [RD2], i.e. this document is an extension of [RD2] and does not repeat algorithms covered in the earlier document, rather builds upon it. As for [RD2], this document is mainly structured along the Glaciers_cci+ product types, i.e. glacier area, elevation change and velocity. While glacier area and elevation changes from DEM differencing and altimetry have individual chapters, velocity as derived from optical and microwave data are summarized in one chapter. According to the Statement of Work (SoW), the Glaciers_cci+ ATBD shall present improvements in algorithms over the existing provisions in terms of the above product areas. The SoW names explicitly improved mapping of debris-covered glaciers using SAR data, determination of surface elevation change using Cryosat-2 and Sentinel-3 altimeter observations, radar interferometric ice velocity measurements, and synergistic use of SAR and optical offset tracking for ice velocity.

Due to the large methodological differences in generating the products, the topics listed above are described differently for each product. However, all Chapters follow the same principle structure (section headings) to keep them comparable.

2. Glacier extent

Satellite data are widely used for repeat mapping of glacier extent as glacier changes are a key climate indicator (e.g. Vaughan et al. 2013, Haeberli et al. 2020) and outlines are required for numerous glaciological and hydrological applications (e.g. calculation of glacier volume, mass balance, run-off, flow velocities). In other words, they are mandatory for most other calculations. The meanwhile freely available optical satellite data at 10 to 30 m spatial resolution (e.g. Sentinel-2, ASTER, Landsat) cover glaciers in most regions in the world, resolve the details required to identify the phenomenon, and allow automated mapping of clean ice using specific spectral bands (e.g. Paul et al. 2016). As ice and snow exhibit strong differences in spectral reflectance between the shortwave infrared (SWIR) and the visible (VIS) or near infrared (NIR), the most common method to map snow and ice is to apply a threshold to a band ratio (e.g. red/SWIR) image [RD2]. The threshold is usually selected to minimize workload for manual corrections. Challenging issues in this regard are ice in shadow (reduced contrast) and under debris cover (hiding the ice). As the latter cannot be mapped with this method, the threshold is usually optimized to provide good results in shadow. Before manual corrections are performed, a noise filter can be applied to the binary glacier mask to remove small snow patches (e.g. Paul et al. 2015, 2020).

Final glacier maps are converted from raster to vector format and the editing is performed in a Geographic Information System (GIS) using contrast stretched versions of different band combinations in the background. At this step commission errors (e.g. wrongly mapped sea ice, water bodies) are manually selected and removed whereas omission errors (missed ice under debris cover or clouds) are identified and corrected. A major point here is that glacier outlines must be spatially complete (closed polygons) in any case. This means that sometimes multi-temporal images have to be used to identify missing parts of a glacier under clouds. A critical point before image processing can start is thus selection of the best possible scenes. These are always a compromise between minimal seasonal snow cover (occurring very late in the summer or at the end of a dry period), cloud cover, and terrain shadows (that are smaller early in summer). As the identification and later mosaicking of such scenes is a considerable effort, other possibilities to facilitate glacier mapping in regions with frequent cloud cover and late seasonal snow have to be found.

In Sections 2.1 to 2.3 we describe related mapping solutions in more detail, not repeating what has already been presented in [RD2]. In Section 2.4 we present possibilities to orthorectify declassified historic satellite images from the Corona mission, that are abundant in some regions of the world and cover the period 1961 to 1980 with 2-5 m resolution panchromatic imagery. This opens the possibility to extend our knowledge about glacier fluctuations several decades into the past. Whereas correcting the highly distorted geometry of Corona images is still a major challenge, processing lines for the Hexagon sensor are already well established, including DEM generation from stereo images (e.g. Holzer et al. 2015, Maurer and Rupper 2015, Zhou et al. 2017 and 2018). Here, we present a new method to process Corona data with a higher degree of automation. Finally, we are presenting a method to automatically detect glacier surges using SAR data.

Contract: 4000127593/19/I-NB

Name: Glaciers_cci+D2.1_ATBD
Version: 1.0
Date: 10.10.2020
Page: 6

Algorithm Theoretical Basis
Document (ATBD)

2.1 Ocean water

2.1.1 Introduction

When mapping glaciers on islands in the Arctic, sea ice is usually misclassified as glacier ice due to its similar spectral properties (see 2.2). However, also clear ocean water is wrongly classified with the band ratio method. To avoid a demanding manual correction, we have developed a method that is excluding ocean water with a further threshold in the blue band.

2.1.2 Methods

The individual steps of the method are illustrated in Fig. 2.1. Dividing the red band (panel a) by the SWIR band (b) gives a ratio image (c) that is after thresholding including all ocean water (d). A further threshold in the blue band classifies ocean water so that it can be separated from the glacier mask (e) resulting in the outlines presented in Fig. 2.1f.
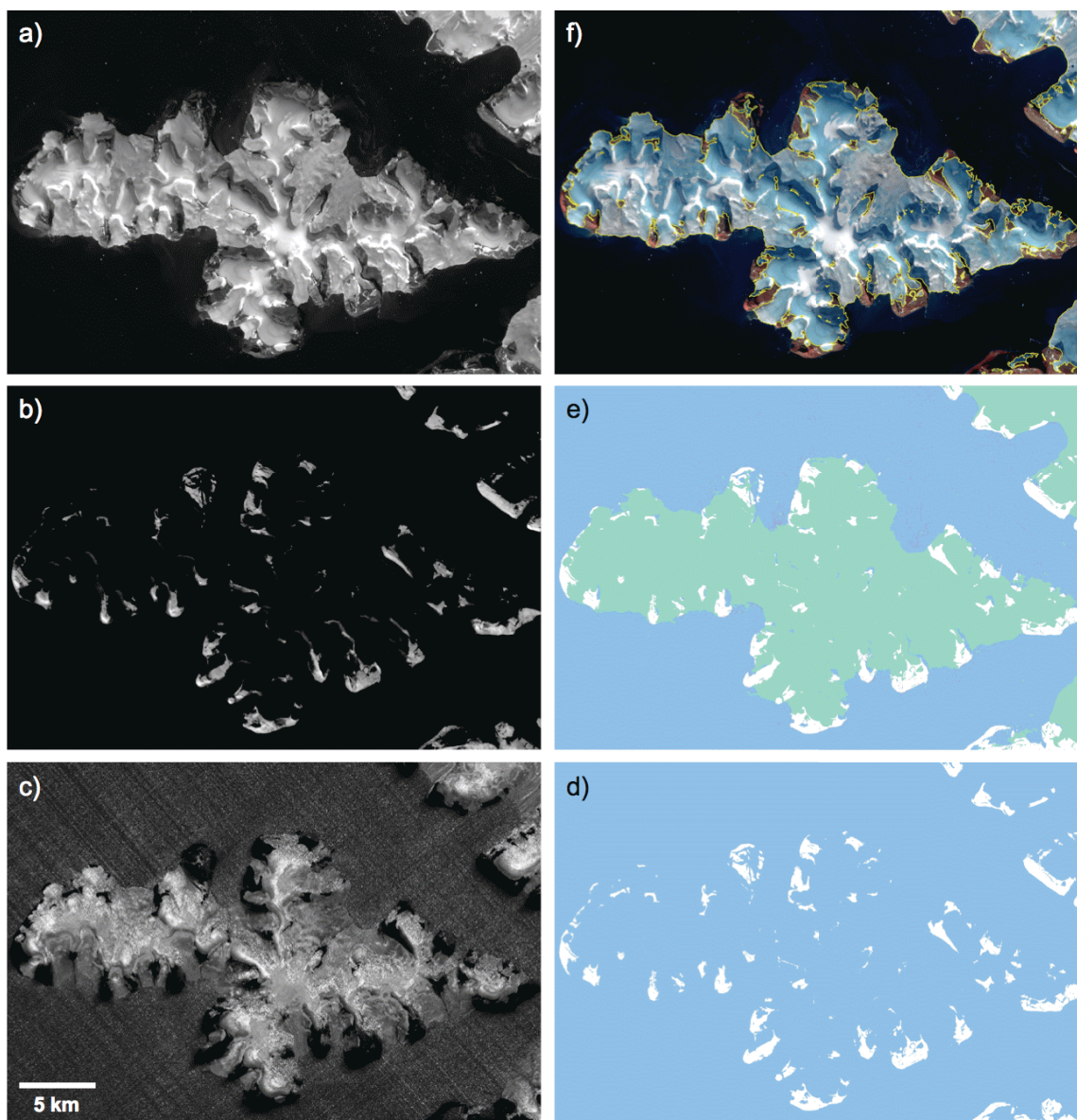

Fig. 2.1: Illustration of the method for Luigi Island in the Franz-Josef-Land archipelago. a) MSI4 (red), b) MSI11 (SWIR), c) ratio MSI4/MSI11, d) glacier map with a threshold of 4, e) ocean water (blue) excluded with a MSI2 threshold of 2100, e) final glacier outlines.

Contract: 4000127593/19/I-NB

Algorithm Theoretical Basis
Document (ATBD)

Name: Glaciers_cci+D2.1_ATBD
Version: 1.0
Date: 10.10.2020
Page: 7

2.1.3 Processing line

As the method for excluding ocean water is applicable to all sensors with a blue, red and SWIR band, we use these names in the processing line given below. The threshold th_1 refers to the value for the band ratio, th_2 to the blue band. For the example with the Sentinel-2 MSI sensor presented above, th_1 is 4.0 and th_2 is 2100. Please note that one of the images used for the band ratio has to be converted to floating point before the division is performed. The method is applied to uncorrected raw data. In pseudo code the processing line is:

```
IF [(red/float(SWIR)) > th₁] and [blue > th₂] then 1 else 0
```

In the classified image the class 1 is 'glacier' and 0 is 'other'. Some experimenting is required to find the best values for th_1 and th_2 but usually they are rather well constrained. The above values might serve as a starting point. Further details on finding the best thresholds are described in the study by Paul et al. (2016).

2.2 Removing clouds, sea ice and seasonal snow

2.2.1 Introduction

Glacier mapping in the Arctic is in particular challenged by frequent cloud cover, long-lasting seasonal snow, sea ice and regionally deep shadows. The resulting mis-classification has to be corrected manually and is approached by processing several overlapping scenes, as acquisitions without clouds and a minimum amount of seasonal snow are rare. The related selection of the best scenes and their independent processing and mosaicking is very time consuming for larger regions.

With the large spatial coverage of Sentinel-2, a very high, near daily temporal resolution of images in Arctic regions results. Assuming that glacier extents do not change much within a few months (surging and calving aside), it makes sense to just process all images available automatically and select the most suitable pixels within this period. This would result in a large reduction of processing time as many time consuming steps (image selection, processing, masking, mosaicking) become obsolete. Such an automated cloud-based image processing approach has been tested here for Svalbard using Google Earth Engine (GEE) and its various possibilities for cloud detection, masking and data filtering.

2.2.2 Methods

As a first step, GEE has to be initiated with the dataset to be investigated (an ImageCollection) and the temporal frame (from - to dates). The resulting image stack is then further processed by filtering. Filters are applied to reduce the image collection based on the characteristics of a satellite scene, e.g. its metadata (cloud cover, image bands), but also to the processing itself to select individual pixels out of a time series (or image stack), e.g. the brightest or darkest one. Due to strong differences in spectral reflectance, such a statistical filtering allows identifying and removing unwanted features from the image stack, e.g. clouds, seasonal snow, sea ice and shadow. We illustrate below the related processing lines for removing clouds and shadow as well as seasonal snow and sea ice for a test site in Svalbard.

2.2.3 Processing line

Removing clouds and shadows

To obtain a cloud-free mosaic for Svalbard, we have at first created an image collection (all Sentinel-2 scenes) and restricted the collection to a two-month period in 2019 (date filter):

```
(var sentinel2_collection = ee.ImageCollection('COPERNICUS/S2')
                 .filterDate('2019-07-05', 2019-08-26)
```

To remove clouds and shadows, a median filter has been applied to the image collection using Earth Engine reducers. This removes clouds (which have a high value) and shadows (which have a low value). When an image collection is reduced using the median reducer, the composite value is the median in each band, over time:

```
var composite = sentinel2_collection.median();
```

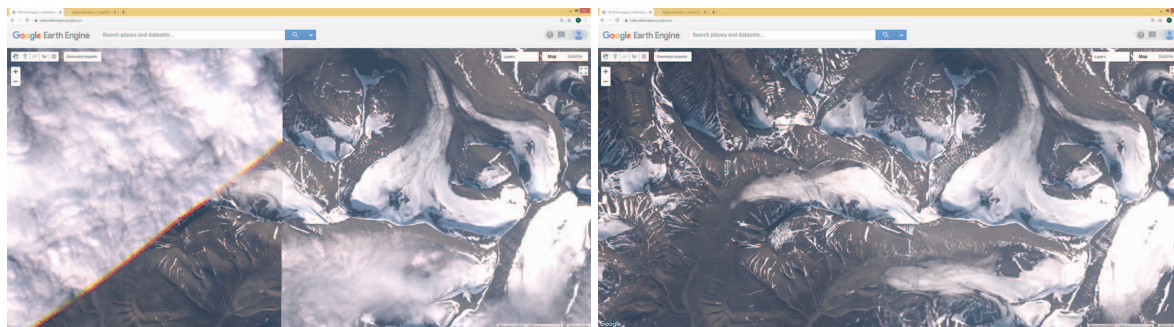As shown in Fig. 2.2, the resulting image composite is cloud free.

Fig. 2.2: Input data preparation with GEE in Svalbard. The left image shows the latest Sentinel 2 scenes for the period applied and the right image the reduced image (median filter) for the same region and the above two-month period.

Removing seasonal snow and sea ice

The principle for the removal of seasonal snow and sea ice is basically the same. Three changes have to be applied in contrast to the algorithm shown above. First, the temporal range (years) needs to be extended to at least two years, second, only summer images are considered (July and August) and third, the minimum instead of the median is applied to the image collection (Figs. 2.3 and 2.4). This allows identifying and removing seasonal snow and sea ice, as they have high pixel values compared to the bare ground or sea (which have low pixel values). The related processing line is:

```
// Sentinel-2 TOA reflectance data for the considered period
var sentinel2_collection = ee.ImageCollection('COPERNICUS/S2')
            .filterDate('2016-07-05', '2018-08-26')
            .filter(ee.Filter.lt('CLOUDY_PIXEL_PERCENTAGE', 20))
            .filter(ee.Filter.calendarRange(7,8,'month'));

// apply the min function to the image collection
var composite = sentinel2_collection.min();
```

This method does not only remove seasonal snow outside glaciers, it also creates an image stack where glacier-covered regions are as dark as possible, i.e. the largest amount of bare ice is visible and the snow line is at its highest position. The resulting image stacks can then be converted to a non-snow or non-sea ice mask.
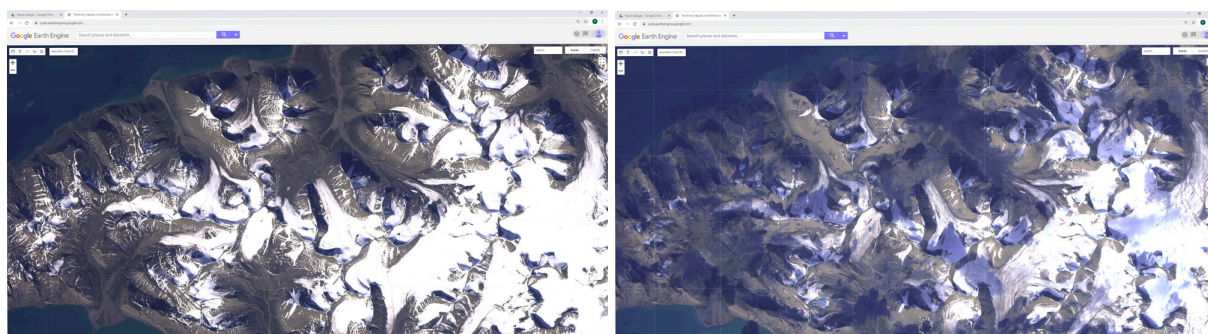
Fig. 2.3: The left panel shows a subset of a Sentinel-2 image (S2A_33XWG_20170802) from one point in time with seasonal snow. The right panel shows the image stack from three summer seasons based on the min function (right), where most of the seasonal snow is effectively removed.
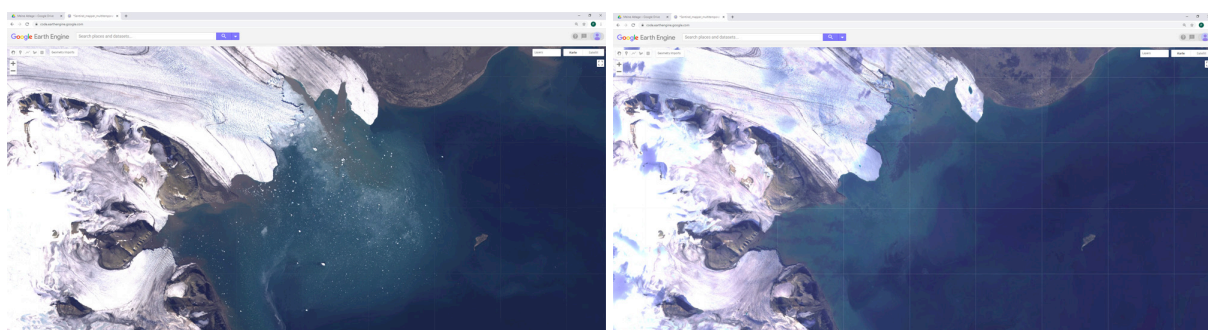

Fig. 2.4: The left panel shows a subset of a Sentinel-2 image (S2A_ 33XWH_20170731) from one point in time with ice bergs floating in front of the calving glacier. The right panel shows the image stack from three summer seasons based on the min function, where all icebergs are effectively removed.

Single day coverage
Due to the large spatial coverage of Sentinel-2, there is a considerable image overlap in Arctic regions. This results in a near complete coverage of large regions by consecutive orbits within a single day. Under specific meteorological circumstances, large regions in the Arctic might be cloud free and can then be mapped in a single day rather than mosaicked from scenes acquired over several decades. Also in this case cloud-based processing with GEE can be applied to avoid downloading hundreds of individual tiles as the region to be processed can be provided by a polygon. This is basically the opposite application of GEE than before, but using the same methods of sensor, region and date filtering. Application of a band ratio to derive a raw glacier extents is possible as well.

glaciers cci

Contract: 4000127593/19/I-NB
Algorithm Theoretical Basis
Document (ATBD)

Name: Glaciers_cci+D2.1_ATBD
Version: 1.0
Date: 10.10.2020
Page: 10

2.3 Mapping debris-covered glaciers

2.3.1 Introduction

Accurate mapping of glacier regions covered by debris is still a major challenge and related to a high workload for manual editing (on-screen digitizing). Accordingly, a large number of methods have been suggested to map extents of debris-covered glaciers automatically from a range of techniques utilizing spectral, thermal, spatial, geomorphometric and other glacier properties. Most of them are based on the fact that debris-covered regions should be flat, free of vegetation and connected to a glacier to distinguish them from steep surrounding rock walls and flat outwash plains covered by the same debris. A method that is based on these simple characteristics was proposed by Paul et al. (2004) and has been integrated in several follow-up studies with different modifications. At a later stage, coherence images from inter-ferometric SAR images acquired in summer were introduced to identify the 'moving' or otherwise changing glacier tongues under debris cover from the loss of coherence (e.g. Frey et al. 2012). This method could also be automatized to a high degree (Atwood et al. 2010) or was combined with other methods (Lippl et al. 2018). Still, the automatically delineated glacier boundaries had to be visually controlled and corrected to provide accurate result, as for example pro-glacial lakes or outwash plains in the glacier forefield are also characterized by a loss of coherence. Moreover, DEMs with good quality are still not available in many regions and the often-used thermal bands have severe caveats (large pixel size, unclear signal in regions with permafrost). In consequence, a really well working 'standard method' does not yet exist.

In the meantime, the 10 m resolution images from Sentinel-2 allow a much better identification of glacier boundaries (Paul et al. 2016) and creation of new glacier inventories can be based on this information alone (Paul et al. 2020). It is also highly recommended to consult very-high resolution imagery as available from Google Earth to aid in the interpretation. This has the caveat that the interpretation of what should belong to a glacier changes with the resolution, i.e. features such as ice-cored lateral moraines become visible and might be included or not, depending on the rules applied (e.g. Mölg et al. 2018). It is thus difficult to use outlines derived from such higher resolution datasets for validation as the rules applied differ. The method we are using to map debris-covered glaciers in Glaciers_cci is thus based on a set of criteria:

(1) Manual editing of raw (clean ice) glacier outlines using contrast enhanced versions of the original satellite image in the background (usually a false colour infrared composite)
(2) Additional guidance from outlines of existing inventories, coherence images and very high-resolution images as available in Google Earth and similar tools
(3) Glaciologic plausibility considerations. These might include checking questions such as 'Does the length/size of the debris-covered part fit to the size of the accumulation region (considering reduced melt under debris cover)?', 'Is this part well-shaded by terrain or exposed to solar radiation?', 'Are ice-cored moraines or rock glaciers present?'.

A major issue to consider for point (2) are differences in the timing, i.e. when the auxiliary data sources are acquired at a different point in time, glacier extents might have changed in the meantime. From the perspective of data processing, it is thus best to focus on the possibilities for processing SAR coherence images from different sensors (e.g. ERS-1/2, JERS-1, Sentinel-1, ALOS-1/2 PALSAR1/2) to have these images available from different points in time. The resulting images can be further processed (e.g. by thresholding and spatial filtering), but we prefer using the raw data as a visual guide to improve visual interpretation.

2.3.2 Methods

In the following we give some background on and describe the basic steps of the interferometric processing (adapted from Frey et al. 2012). The degree of coherence is a measure of the phase noise of the interferogram. It depends on sensor parameters (wavelength, polarization, system noise, slant range resolution), parameters related to the imaging geometry (interferometric baseline, local incidence angle), and target parameters. Volume scattering and temporal change (i.e. random motion of the scatterers, change of the scatterers) decrease the degree of coherence. The system- and geometry-dependent effects can be taken into account by appropriate interferometric processing. The decorrelation caused by volume scattering and temporal change, on the other hand, is important to characterize the target properties. During summer time, most of the seasonal snow has disappeared and ice flow and melting are the main factors of surface-geometry changes, which lead to a decrease of the coherence over flowing glacier ice (Fig. 2.5). As also some other regions near glaciers (lakes) show a low coherence, mapping with a simple threshold applied to the coherence values does not work.
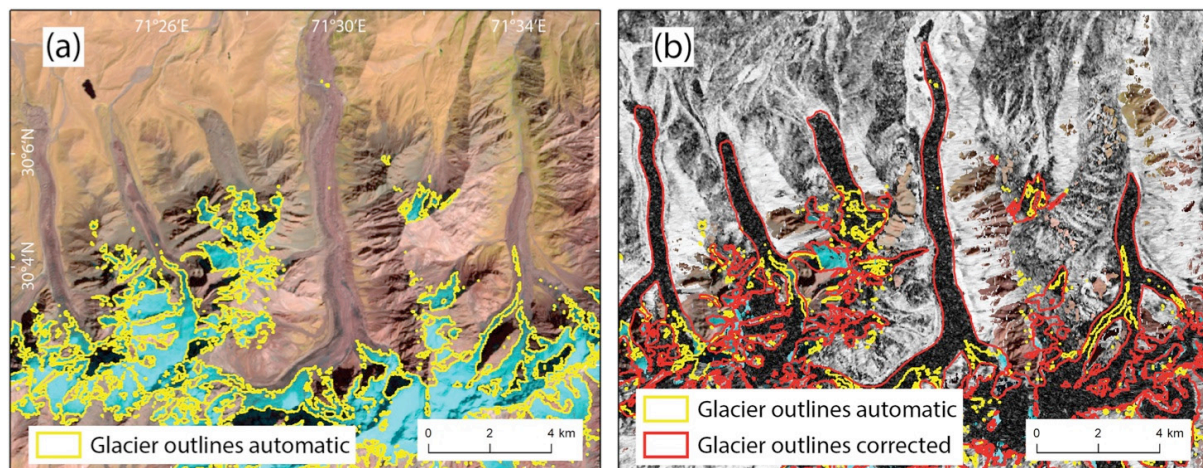

Fig. 2.5: (a) False-colour image with raw glacier outlines (yellow). (b) PALSAR coherence images with raw and corrected (red) outlines. The decorrelated pixels are near black. Image taken from Mölg et al. (2018).

The SAR processing includes radiometric calibration for the antenna gain and slant range distance, radio frequency interference filtering, and common band filtering of the azimuth and range spectra. The resulting single look complex (SLC) images should be well focused to produce interferograms of high quality after accurate co-registration of master and slave images (e.g. Ulaby et al. 1982). The interferometric processing combines pairs of SLC images at HH-polarization into an interferogram. Because of rugged areas, a simulated phase image, which corresponds to the topographic phase, should be computed from the best available DEM and then subtracted from the interferometric phase. For coherence estimation an adaptive window size can be used. In the first step, the coherence is estimated with a fixed, relatively small window size. In the second step, the window size is determined based on the first estimate, applying larger windows in order to estimate lower coherence. The estimator window size varies typically between 3 x 3 and 9 x 9 pixels for interferogram with 4 azimuth-looks. In addition, a weighting function, decreasing linearly with increasing distance, was applied (Wegmüller and Werner 1996). With this procedure reliable values at the pixel level can be found without compromising the spatial resolution. The resulting terrain-corrected and geocoded coherence images are finally combined with a mask considering regions with layover and radar shadow as well as possible DEM voids.

Figure 2.6 shows a comparison of coherence images as derived from different sensors for the glaciers in the central Karakoram. Whereas the PALSAR coherence image has slightly better contrast, it has also more data voids. However, these are mostly located outside of glaciers.
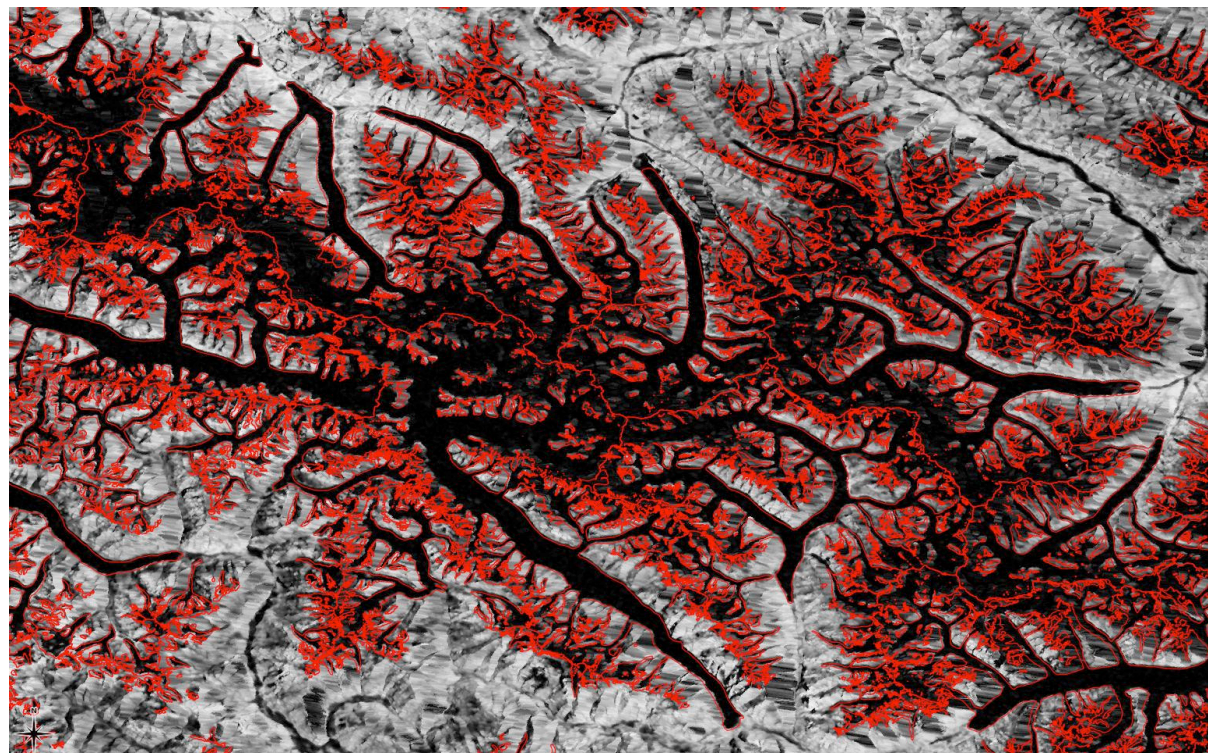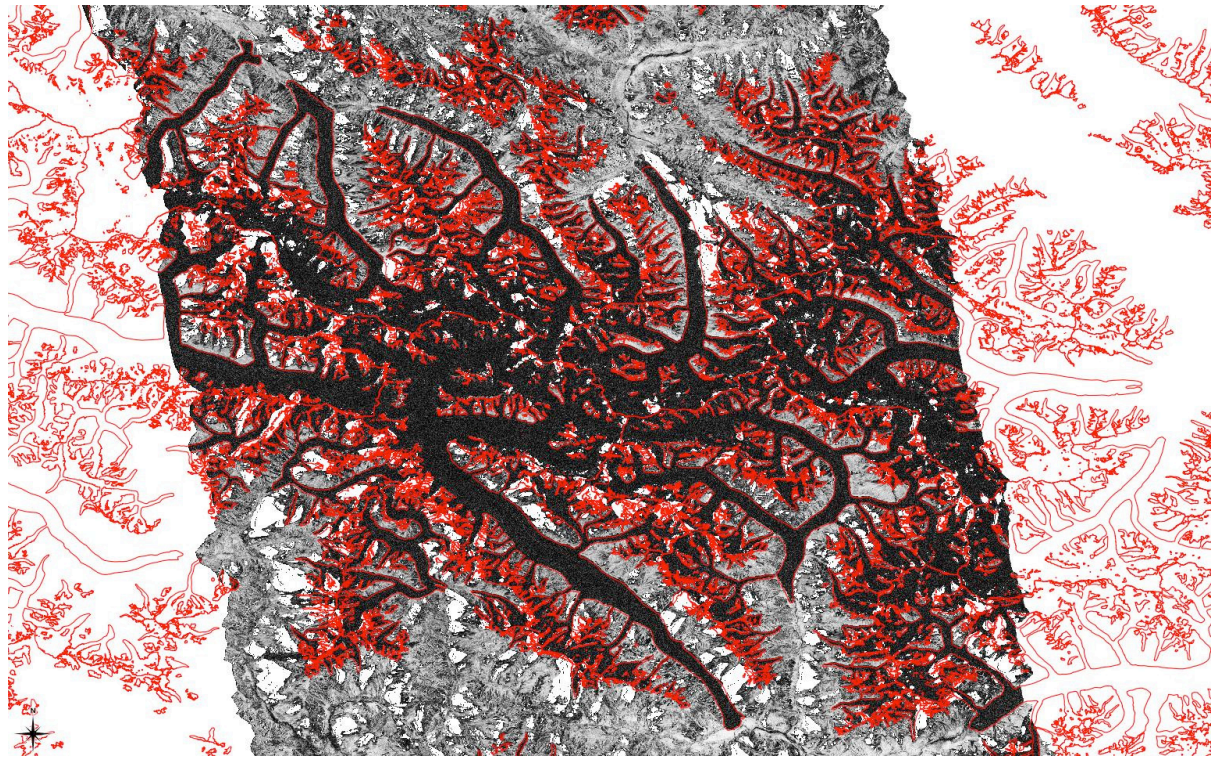

Fig. 2.6: Coherence images derived for the central Karakoram from (top) ALOS1-PALSAR1 and (bottom) Sentinel-1.

2.3.3 Processing line

In Fig. 2.7 the principle processing line for the creation of coherence images (applicable to different sensors) is shown. As mentioned above, these provide additional guidance for the interpretation of debris-covered glaciers, but are not used directly.
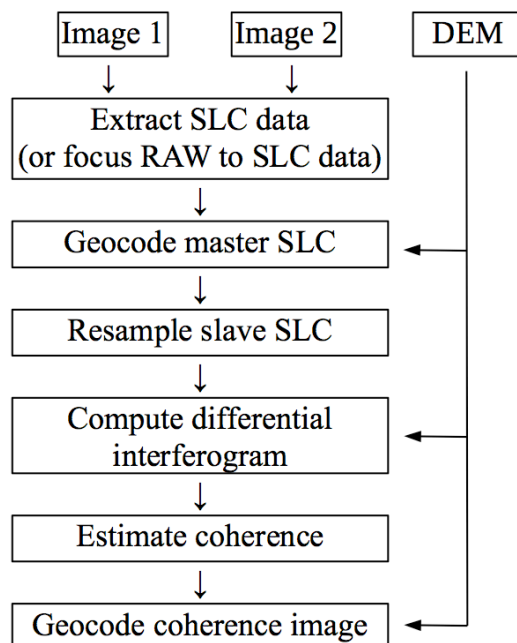

Fig. 2.7: Generalized processing line to create coherence images from SAR image pairs.

2.4 Processing of Corona images

2.4.1 Introduction

Images from Corona and Hexagon offer the possibility to extend the time series of observed glacier changes substantially, in extent as well as for elevation changes (e.g. Maurer et al. 2019, Goerlich et al. 2017). However, processing of the digitized films is challenging as these have several complex geometric distortions. In this section we focus on the processing of Corona images, which have a more complex geometry than Hexagon images; their processing is discussed in Section 2.5. The goal here is two-fold: (i) removing image distortions to create an orthoimage that can be used to determine quantitative changes, and (ii) DEM creation from Corona stereo pairs. The usual processing line for stereo images starts with (ii) as a DEM is required to create an orthoimage and is thus described first. As (i), the orthorectification, can also be performed with an external DEM, this is described additionally.

The Corona Satellites were part of the Central Intelligence Agency Keyhole program (KH-4, KH-4A. KH-4B). The first KH-4 mission was launched in February 1959 and the first images were received in August 1960. The Corona missions ended in May 1972 and delivered ~800.000 scenes of mainly former UDSSR territory. The images were taken by two panchromatic cameras tilted 15° forward and backward and measure 5.5 cm x 75.7 cm, which leads to a coverage of around 17 km x 232 km. The coverage varies due to orbital and terrain height. The ground resolution of the images thus varies between 1.8 m and 7.6 m.

Due to the high resolution of the panchromatic images, many applications are possible. Unfortunately, processing the images needs to solve several challenges. The most important are: (a) the highly variable and very specific image geometry, (b) changing camera parameters due to the continuous development of the cameras, (c) the manual scanning by USGS with a scanner that introduced further distortions (e.g. the scanner head might have moved with variable speed), and (d) the age of the images and the long storage duration, which leads to random distortions within the image. Collectively, these points make it very difficult and time consuming to generate orthoimages and useful DEMs from Corona. As an example for (c), Fig. 2.8 shows the results of unsuccessful density slicing (tested for glacier extent mapping). The image has systematic (wave-like) brightness variations at both image boundaries.
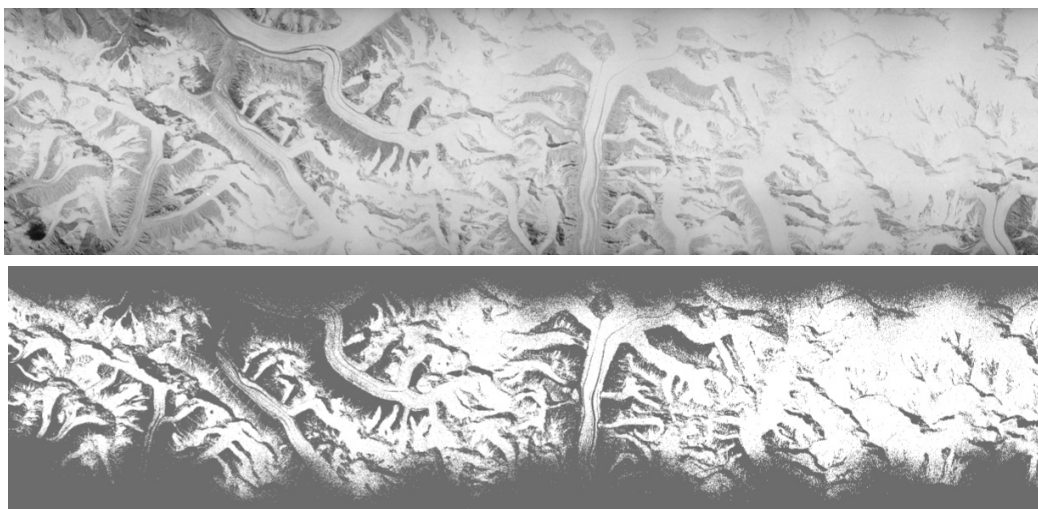

Fig. 2.8: Original quarter of a Corona stripe (top) and result of density slicing (bottom).

Processing of Corona images thus requires using software that includes the Corona panoramic image geometry (averaged geometry). To our knowledge, only RSG (Remote Sensing Software Graz) developed by Joanneum Research Graz includes this geometry. The Corona geometry was implemented in a relatively early state of the software and was unfortunately not further developed. However, RSG provides also all photogrammetric features and algorithms to compute DEMs from stereo images and is primarily script based (some functions are not available via the GUI). To generate orthoimages and DEMs from Corona data the two (forward and backward) images with an overlapping area are needed. Further, reference data for GCP (Ground Control Point) measuring in horizontal and vertical dimension is necessary (orthoimages and DEM).

2.4.2 Methods

The processing of a Corona stereo image pair can be separated in three parts: pre-, main- and post-processing. In the pre-processing, all data have to be prepared. This includes the alignment of the four image stripes (all scenes come in four single overlapping image parts labelled a, b, c, d) manually and to lower the resolution from 7 to 14 micron because the image quality is usually too low for a reasonable processing at 7 microns. Unfortunately, the four single image parts do not fit always properly together. This means they might need to be slightly rotated or scaled up before they can be merged to a single string. Figure 2.9 provides an example of the 4 parts and the overlapping regions. Afterwards it might be necessary to define subsets if not the full scene should be processed. This is also recommended for full scene processing (using three overlapping parts) because the image distortion model can be better applied to smaller subsets rather than to a full scene.
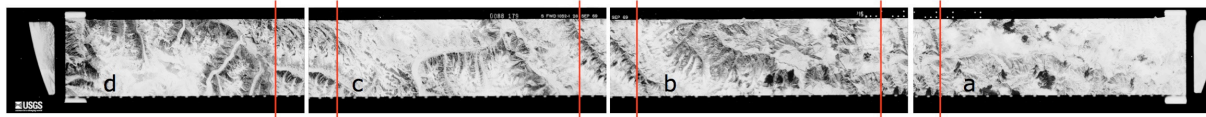
Fig. 2.9: The four parts of a Corona stripe that have to be mosaicked before the processing. Red lines mark the regions of overlap.

Once the input images are prepared, they have to be imported to RSG with their corresponding characteristics (sensor, subsensor, subset definitions) and further definitions of the image have to be defined (flying direction, focal length, pixel size and flying height). In a next step, the stereo model is set up as usually done in standard stereo-photogrammetric processing. Images are oriented to a geographic reference coordinate system via ground control points (GCPs). The GCP collection should be as evenly distributed as possible (horizontally and vertically) with about 20 GCPs per subset. The GCPs should be placed on stable terrain. Ideally, GCPs occurring in both images should be used as tie-points (TPs) in the next step as well. The images are then geometrically adjusted (all values that are unreliable have to be adjusted) showing residuals for all GCPs. These values should be below 5 pixels, otherwise the respective GCP have to be measured again or deleted.

The now geometrically adjusted images have to be added to the stereo block and a geometric adjustment of the block with both images is performed. The results should be the same as in the individual adjustment. To better adjust both images to each other, TPs have to be collected. This is done automatically and should reveal around 1000 TPs followed by polynomial adjustment as a basis for the epipolar registration. In a true epipolar geometry corresponding points are situated on straight lines (epipolar lines). This makes the image matching process more stable and faster. Important is that the Y-parallax is comparably low while the X-parallax can show higher values. Unfortunately, the epipolar registration is almost impossible with Corona due to the problems mentioned above. Therefore, corresponding pixels of both images are searched within a certain window rather than along a line. This approach has a higher error rate and a much higher computational effort, though.

To optimize the matching process, top-level disparities are calculated for both images from the vertical reference DEM (Fig. 2.10). The output raster shows predictions about shifts regarding the viewing angle and the topography. The matching process takes this information as input and can reduce the search radius for corresponding pixels in both images. The better the alignments worked beforehand, the smaller the search window can be chosen, improving both the processing time and quality. The output raster is a disparity raster with 4 bands that are used later to calculate the height of each pixel (Fig. 2.11). The height raster is then further interpolated to a final DEM. The resolution of this DEM can be chosen freely but should be around three times the image resolution.

In the post-processing, DEMs from individual Corona stripes have to be mosaicked, possible artefacts need to be detected and corrected, and data voids need to be interpolated or filled. For these latter steps as well as DEM subtraction (to determine elevation changes), the DEM has to be co-registered to a master DEM. This has to be done outside RSG, e.g. following Nuth and Kääb (2011). The DEM can also be used to orthorectify the Corona images. This process follows the basic photogrammetric approach to generate orthoimages. It delivers an as good as possible orthoimage of the respective Corona scene with data voids at the pixels that the matching process was not able to find a corresponding pixel in the other stereo image.

Contract: 4000127593/19/I-NB

Algorithm Theoretical Basis
Document (ATBD)

Name: Glaciers_cci+D2.1_ATBD
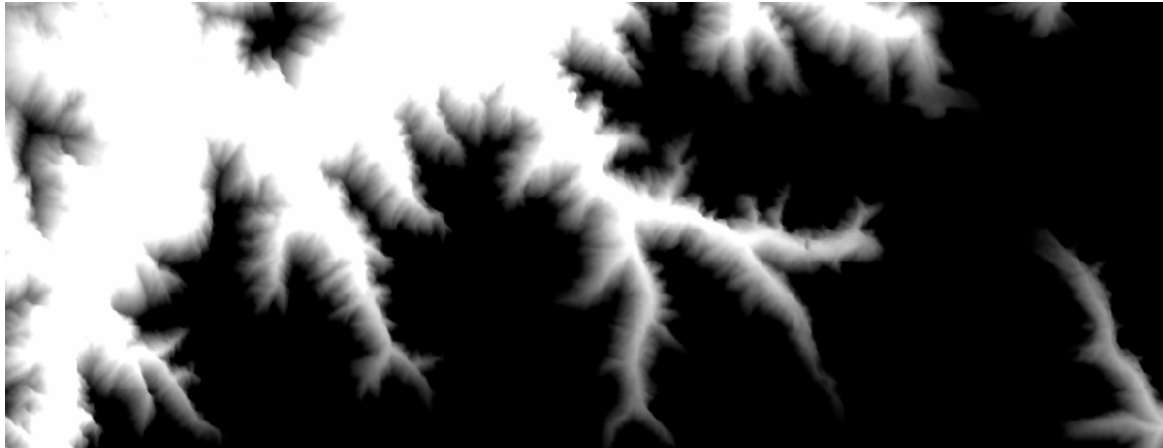Version: 1.0
Date: 10.10.2020
Page: 16

Fig. 2.10: Top level disparities of a DEM for improving the search radius of the mathing process. Bright areas show lower elevations and dark areas higher elevations.
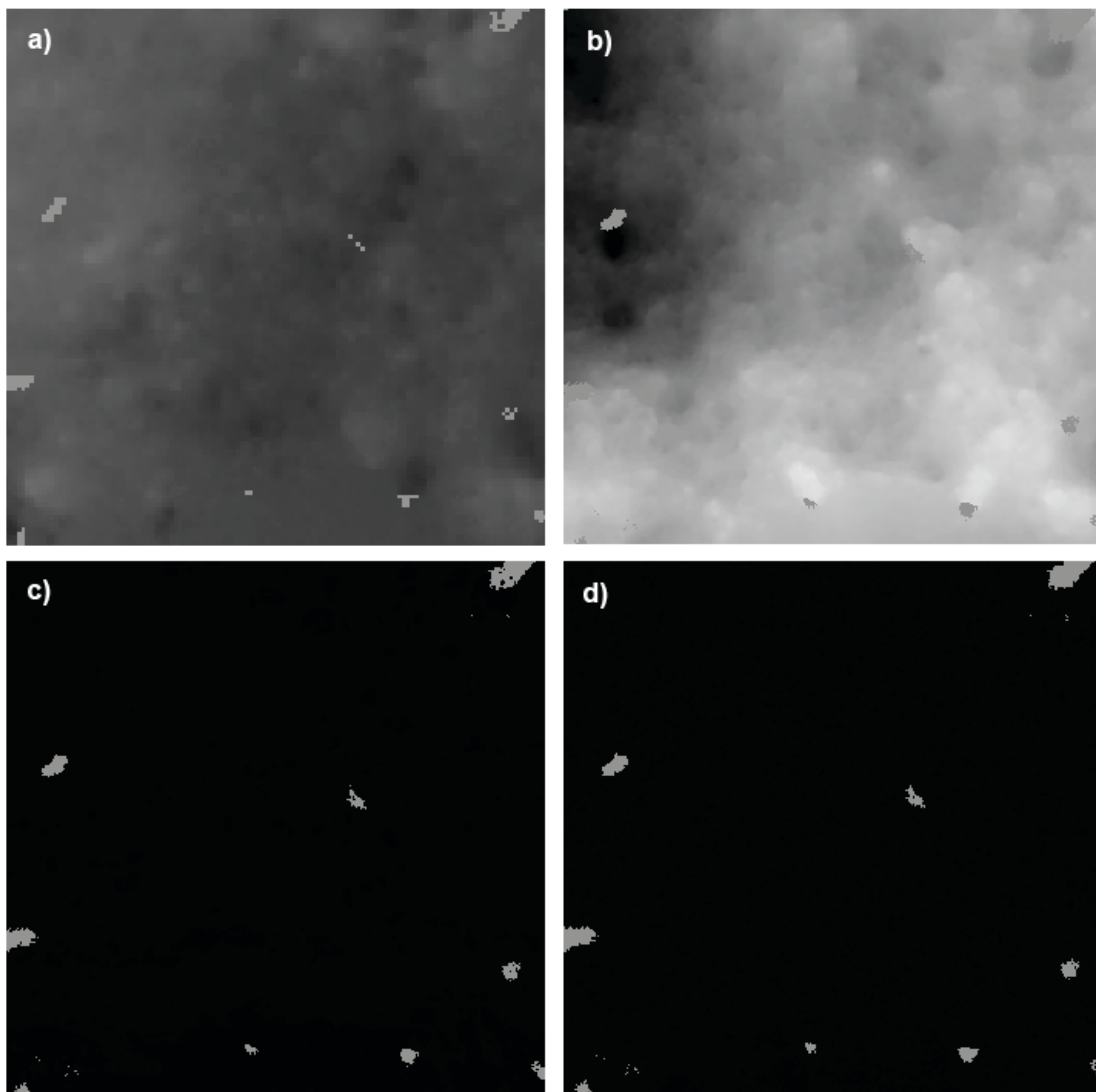

Fig. 2.11: Disparity map extracts. a) Band 1: disparities in column direction; b) Band 2: in line direction; c) Band 3: feature distances; d) Band 4 - back-matching distances.

Another option to generate orthoimages from Corona imagery is to use another DEM than the Corona generated one. Therefore, all steps before the top-level disparity computation have to be done in the same way. This ensures that the correct geolocation of the Corona image and integration in the Corona model of RSG. Then the orthorectification process can be done the same way but using another DEM such as ASTER GDEM or SRTM. The main advantage is that a DEM without data voids (or at least less than the Corona DEMs) can be chosen to generate complete orthoimages. Further, it skips the top-level disparity processing and the matching process that are highly time consuming and need a lot of processing power.

The disadvantage is mainly the usually incorrect surface elevations of glaciers, which might have changed over the years. This results in wrongly projected pixels resulting in a lateral displacement of pixel positions. How large this shift is depends on the elevation difference between the acquisition year of the Corona scene and the acquisition date of the DEM. Usually it affects the glacier tongues only (also the main interest of the orthophoto analysis) and is primarily significant on surge-type glaciers, where the surface elevation difference between a few years can be several 100 m (Kääb et al. 2016).

2.4.3 Processing line

As a generalized overview, Fig. 2.12 presents a schematic processing line for othorectification and DEM creation using Corona images.
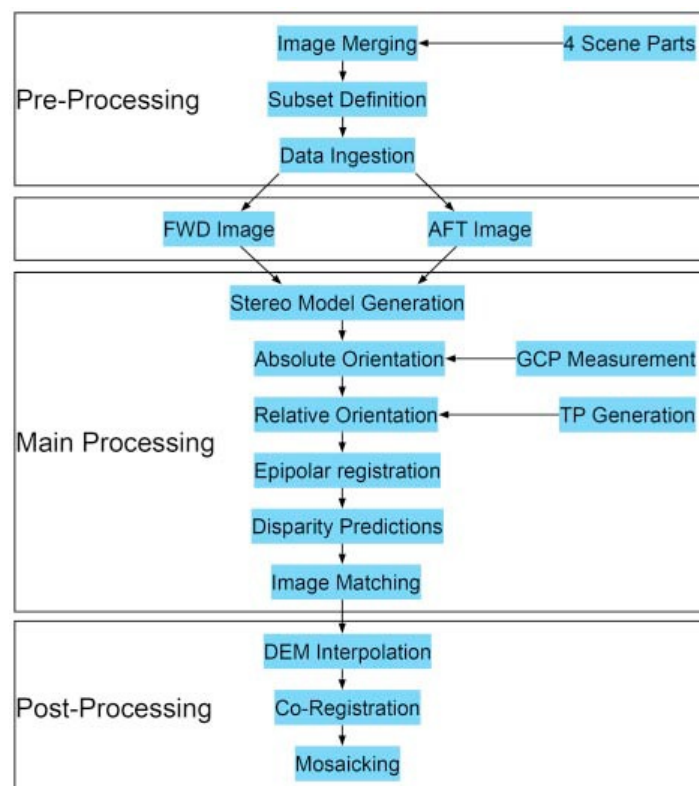

Fig. 2.12: Corona stereo image processing line using RSG.

glaciers cci

Contract: 4000127593/19/I-NB
Algorithm Theoretical Basis
Document (ATBD)

Name: Glaciers_cci+D2.1_ATBD
Version: 1.0
Date: 10.10.2020
Page: 18

2.5 Detection of glacier surges

2.5.1 Introduction

Glacier surges are of interest for a range of reasons. They constitute an instability in glacier flow and their understanding significantly contributes to a better understanding of glacier motion. Glacier surges pose natural hazards, either directly by inundating land and destroying infrastructure, or, typically more severe, by damming up rivers and causing flood hazards once their ice dams break (e.g. Harrison et al. 2015, Round et al. 2017). Also in glacier monitoring, glacier surges need to be accounted for. They cause disturbances in the glacier's mass balance and elevation changes, which makes surge-type glaciers to differ from a regional climatic mass balance signal (e.g. Gardelle et al. 2012). Similarly, glacier surges often cause non-climatic advances and need to be filtered out of climatic series of glacier length and area (Yde and Paasche 2010).

Glacier surges are so far identified in various ways such as from morphological features like looped moraines (e.g. Herreid and Tuffer 2016) or animations (e.g. Paul 2015) in high-resolution optical data, from visual interpretation of enhanced crevassing or shear margins (using very-high resolution optical data) or from time-series of glacier velocities (Chapter 4) when these measurements show strongly enhanced ice flow (e.g. Paul et al. 2017, Quincey et al. 2015).

Within Glaciers_cci+ we develop a novel method that supplements above existing methods, and can be efficiently employed in a systematic way over large or global scales. It is important to note that the method is meant as a tool for systematic initial surge detection, in order to focus and prepare for other methods to then investigate surges in detail, or else account for them (e.g. by excluding them from climate-related glacier monitoring).

2.5.2 Methods

The method introduced builds on the fact that most glacier surges lead to enhanced glacier crevassing, which then enhances the backscatter in SAR images (Fig. 2.13). To exploit this behaviour we analyse stacks of Sentinel-1 IW mode SAR backscatter images within Google Earth Engine (GEE; see Section 2.2). A number of ways could be employed to detect backscatter changes over time in such SAR image series. Here, we use the pixel-wise backscatter stack maxima for winter stacks and compare them annually, from winter to winter. Focus on winter images minimizes disturbing summer effects such as surface melt, changes in micro-roughness, formation of superimposed ice, etc. The annual comparison will then be made visually, based on flicker images, differences or normalized differences between two years/winters where strong changes in backscatter are well recognizable (Fig. 2.14).

Fig. 2.13: Sentinel-1 VH backscatter images over Negribreen (bright area middle left) and Sonklarbreen (bright area upper right), Svalbard. Upper image: 2018-0323, lower image: 2020-03-18. While the strong crevassing by the ongoing Negribreen surge (Haga et al. 2020) is visible by strong backscatter in both winters, a starting surge of parts of Sonklarbreen causes strong backscatter only in the 2020 data.

Contract: 4000127593/19/I-NB
Algorithm Theoretical Basis
Document (ATBD)

Name: Glaciers_cci+D2.1_ATBD
Version: 1.0
Date: 10.10.2020
Page: 20

Fig. 2.14: Surge detection over parts of Karakoram between winters 2018 and 2019. Left: Normalized differences between Sentinel-1 VH winter stack maxima of the two years. Right: as left but masked by the RGI outlines. White zones indicate a starting surge (lower blue marker), black zones a declining surge (upper marker).

2.5.3 Processing line

GEE is introduced in Section 2.2. Development and testing of the method is ongoing, but in our current implementation the processing line to visualize surges is depicted in Fig. 2.15:

Fig. 2.15: Processing line for detection of glacier surges with SAR data.

glaciers cci

Contract: 4000127593/19/I-NB

Algorithm Theoretical Basis
Document (ATBD)

Name: Glaciers_cci+D2.1_ATBD
Version: 1.0
Date: 10.10.2020
Page: 21

3. Elevation change

3.1 Radar penetration collection

3.1.1 Introduction

Radar elevation data sets such as SRTM, TanDEM-X, but also altimeter data such as from Cryosat-2, are affected by radar penetration causing the phase centre, to which an elevation value refers, to be not necessary on the surface. In particular dh/dt measurements are affected by radar penetration, as it typically varies over time, causing an unwanted additional dh between elevation data sets from different times. Both are affected, comparisons between radar elevation data and comparisons between one radar elevation dataset and one optical photogrammetric elevation dataset (e.g. ASTER, ASTER GDEM, HMA DEM, Arctic DEM).

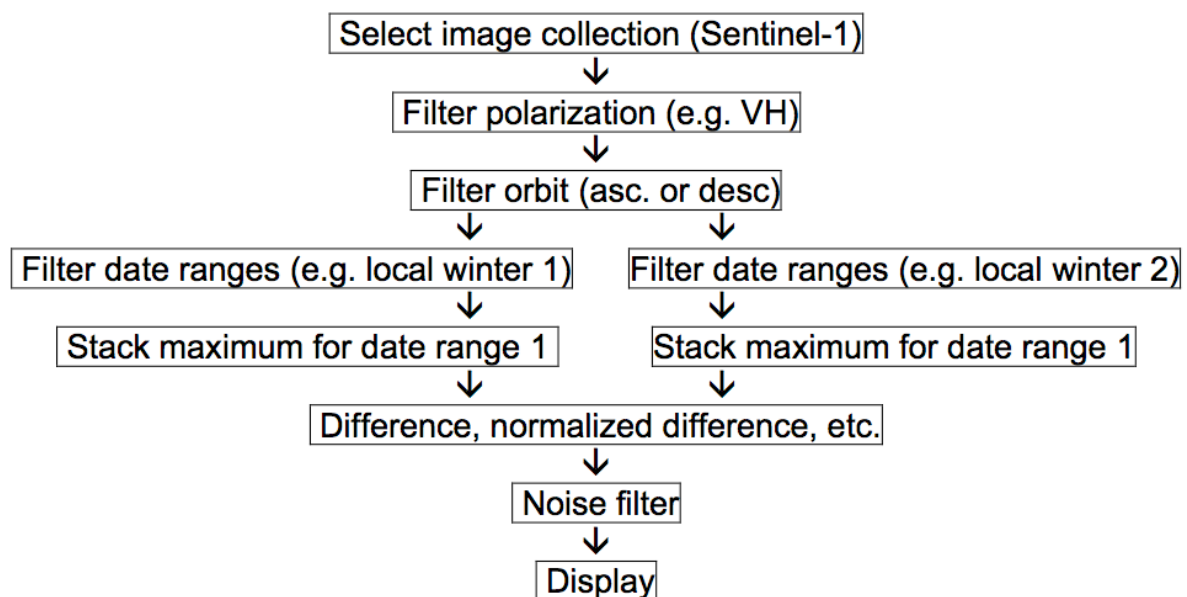Not least the TanDEM-X DEM has a large potential to provide glacier elevation changes for ten-thousands of glaciers when combined with the SRTM DEM. However, the C- and X-Band waves penetrate into snow and firn by several (unknown) metres (Kääb et al. 2012, Dehecq et al. 2016). Proper correction of this penetration is difficult, impacting on the quality of the derived results. With the now available very high-resolution (2 m) ArcticDEM it is possible to investigate the penetration issue more systematically and provide suggestions for a possible correction (e.g. von Albedyll et al. 2018).

One of the major complications of quantifying radar penetration into snow an ice is that it is highly variable over time, depending both on the specific conditions at the time of acquisitions (e.g. surface melt, volume conditions) and the evolution of the penetration volume over weeks and months (e.g. development of ice layers and ice lenses).

Quantification of radar penetration and development of corrections, or uncertainty quantifications, are much complicated by the lack of large-scale spatially-resolved measurements of penetration depths. The best data sets for quantifying penetration depths are as simultaneous as possible elevation differences between radar elevation data and optical elevation data sets from optical photogrammetry or laser. The increasing availability of optical elevation data such as from satellite stereo (HMA DEM, Arctic DEM, etc.) and satellite laser (ICESat-2) offer now much improved possibilities to make progress in quantification, modelling and possibly correcting radar elevation data for penetration into snow and ice.

Glacier_cci+ aims thus at producing and compiling a collection of elevation differences between radar and optical elevation data in order to support and propose strategies to correct for radar penetration, or improve ways to quantify errors imposed on geodetic glacier mass balances by radar penetration.

3.1.2 Methods

The methods used are equivalent to DEM differencing [RD2] or the surface modelling approach in Section 3.3 with the addition that:
- The two elevation datasets should be acquired as close to each other as possible, or acquired under similar conditions (e.g. both winter season; zones of little glacier changes)
- Where available, SAR backscatter images associated with the radar elevation data set, or near-simultaneous with it, can be used to characterise radar surface conditions, in particular surface melt (=low backscatter) that should point to little radar penetration.

Contract: 4000127593/19/I-NB
Algorithm Theoretical Basis
Document (ATBD)

Name: Glaciers_cci+D2.1_ATBD
Version: 1.0
Date: 10.10.2020
Page: 22

3.1.3   Processing line

Equivalent to DEM differencing [RD2] or the surface modelling approach in Section 3.3

3.2   Seasonal and historic dh/dt from altimetry sensors

3.2.1   Introduction

Cryosat-2 has already been used to determine trends in surface elevation changes over larger glaciers and ice caps (e.g. Foresta et al. 2016). With the sub-seasonal temporal resolution of Cryosat-2 and other RADAR altimeters such as SARAL (Sentinel-3) it might be possible to obtain ablation and accumulation rates over larger glaciers and ice caps on a regular basis. The development of related algorithms might require adding flow velocities.

Historical altimetry data from ERS1, ERS2, Envisat and CryoSat-2 have been cross-calibrated to produce long-period time series of trends for Antarctic ice sheet and ice shelf regions (e.g. Shepherd et al. 2019). The same method will be applied here to glaciers of interest.

3.2.2   Methods

Datasets from each mission are prepared separately, and are then cross-calibrated to provide a historical record. A surface modelling method is used.

3.2.2.1   Single mission processing

All altimetry data stems from examination of radar echo waveforms and their transit times. Each mission provides measurements of time, location of echoing point, surface elevation at that point, backscatter power, and satellite heading (i.e. whether the orbit is ascending or descending at measurement time). The location and surface elevation are corrected for ground slope effects when possible, and the surface elevation is also corrected for geophysical effects. The geophysical corrections provided are dry tropospheric, wet tropospheric, ionospheric, solid earth tide, pole tide and ocean loading tide.

For each region of interest, data are gridded geographically, and time-series of elevation change in each cell are produced. First, a surface model is fitted to the data, and residual elevation anomalies derived. Then, for the radar altimetry missions, a second model is fitted to remove short-period fluctuations correlated with backscatter power changes. Finally, correction for glacial isostatic adjustment is applied to each elevation in the resulting time-series.

3.2.2.2   Multi-mission cross-calibration

As in the single mission processing, each grid cell is treated separately. Multiple linear regression is used to fit a cubic polynomial model to the combined time-series of all missions, calculating a bias coefficient for each individual mission. These biases are applied to the initial time-series to perform the cross-calibration.

3.2.2.3   Surface elevation change rate

The cross-calibrated time-series in each cell give a record of surface elevation change, dh. The surface elevation change rate, dh/dt, is derived from a fitted linear model.

Contract: 4000127593/19/I-NB
Algorithm Theoretical Basis
Document (ATBD)

Name: Glaciers_cci+D2.1_ATBD
Version: 1.0
Date: 10.10.2020
Page: 23

3.2.3 Processing line

3.2.3.1 Regions of interest and grid projection

The four regions of interest are Svalbard, Novaya Zemlya, Franz-Josef-Land and Severnaya Zemlya. In each region a 1km polar stereographic grid is imposed. All use the same projection, EPSG 3413, which is polar stereographic, central meridian 45W, latitude of origin 70N, ellipsoid WGS84.

Svalbard: grid size 460 x 600, extreme bottom left at x = 900km, y = -800km
Novaya Zemlya: grid size 650 x 500, extreme bottom left at x = 1250km, y = 150km
Franz-Josef-Land: grid size 350 x 450, extreme bottom left at x = 800km, y = -50km
Severnaya Zemlya: grid size 250 x 450, extreme bottom left at x = 550km, y = 650km

3.2.3.2 Ingestion

Radar altimetry missions used and their baselines are;
ERS1 – Reaper
ERS2 – Reaper
EnviSat - GDRv3
CryoSat-2 – baseline D, SARIn mode
Sentinel 3A – SR_2_LAN_NT baseline 4
Sentinel 3B – SR_2_LAN_NT baseline 4

Two laser altimetry mission datasets are available for validation;
ICESat 1 – GLAH 12
ICESat 2 – ATL06 baseline 3

Level 2 data is used, except for CryoSat-2, which uses L2i. Data from all surfaces is used, as often, especially for ERS1 and 2, the land masks supplied in the data products are at too low resolution to successfully separate land ice and ocean over small areas.

All available data files over the regions of interest are read in and data are extracted. The data is binned according to the grids in section 3.3.3.1 above. Variables extracted are:
- Time
- Surface elevation
    - Provided with slope-correction applied
    - In all missions except EnviSat provided with geophysical corrections applied. EnviSat supplies the correction separately, and they are added during ingestion. The corrections are dry tropospheric, wet tropospheric, ionospheric, solid earth tide, pole tide and ocean loading tide.
- Location, provided with slope-correction applied
- Backscatter power
- Satellite heading

3.2.3.3 Single-mission, single-cell surface elevation change timeseries

The data from each mission and each geographic grid cell is processed separately at this stage. A cell is only processed if it contains at least 15 datapoints.

First, a quadratic surface model is fitted to the cell data, using a Levenberg-Marquardt least squares fitting method. The model equation is:

$$z(x, y, h) = z_m + a_0 x + a_1 y + a_2 x^2 + a_3 y^2 + a_4 xy + a_5 h + a_6 t$$

where z is height, x is the polar stereographic easting coordinate, y is the polar stereographic northing coordinate, h is the satellite heading (set as binary), and t is the time of the elevation measurement. The coefficients are derived using the least squares fit. Measured heights more than two standard deviations from the modelled height are discarded, and this procedure was repeated until either no outliers or fewer than fifteen data points remain (in which case the results in the grid cell are not used).

The modelled surface is removed from the elevation data to provide a time-series of elevation anomalies. A second model is fitted to the results to remove residual, short-period fluctuations correlated with changes in backscattered power that arise in radar altimeter measurements over continental ice sheets (Wingham et al., 1998). Laser altimeters do not show this effect, so this step is omitted for ICESat-1 and 2. This second model is applied in a separate step to ensure that it does not interfere with the spatial and temporal elevation fit. It is again determined using a Levenberg-Marquardt least squares, with an equation of the form:

$$p = a_0 + a_1 t + a_2 h$$

where p is the backscatter power, t is the time of the measurement, and h is the satellite heading. A time series of backscatter power is reconstructed using this model fit and the anomalies, and 5-year trends in dp/dz are computed over a 5-year (if possible) or 2-year period by correlating the power and elevation anomaly time-series. The periods are chosen by their relative stability in terms of orbit manoeuvres, outages and on-board changes. The fitting procedure is again iterated to remove outliers more than two standard deviations from the modelled value, either until there are none or more than three iterations have occurred (in which case the results are not used).

The component of each elevation due to the power fluctuations is then removed, to produce a time-series of corrected surface elevation changes – the elevation anomalies. The elevation change data are averaged over 30-day epochs. A correction for glacial isostatic uplift is applied to each data point, using the ICE-5G model (Peltier, 2004).

3.2.3.4 Single-cell multi-mission cross-calibration

The data from each geographic grid cell is processed separately at this stage.

Multiple linear regression is used to derive the cross-calibration ('bias') values necessary to produce a continuous multi-mission time-series (for general details see Tabachnick and Fidell 2019). It is assumed that the time-series follows a cubic polynomial form over time. The independent variables are

- time
- time squared
- time cubed
- a flag array for each mission except the first.

Contract: 4000127593/19/I-NB

Algorithm Theoretical Basis
Document (ATBD)

Name: Glaciers_cci+D2.1_ATBD
Version: 1.0
Date: 10.10.2020
Page: 25

The regression produces a coefficient for each independent variable. The coefficients for each mission are the bias values. The first mission is unbiased, and the rest biased with respect to it. When these biases are applied to the data, it clusters around the cubic polynomial model, as seen in Fig 3.1. This shows an example from the Copernicus Climate Change Service Antarctic Ice Sheet surface elevation change product, with six mission time-series in order, from a grid cell inland of the Thwaites Glacier. On the left they are not cross-calibrated. On the right cross-calibration has been applied so that the earliest mission's position is unchanged. The model polynomial is also shown, as a solid line.
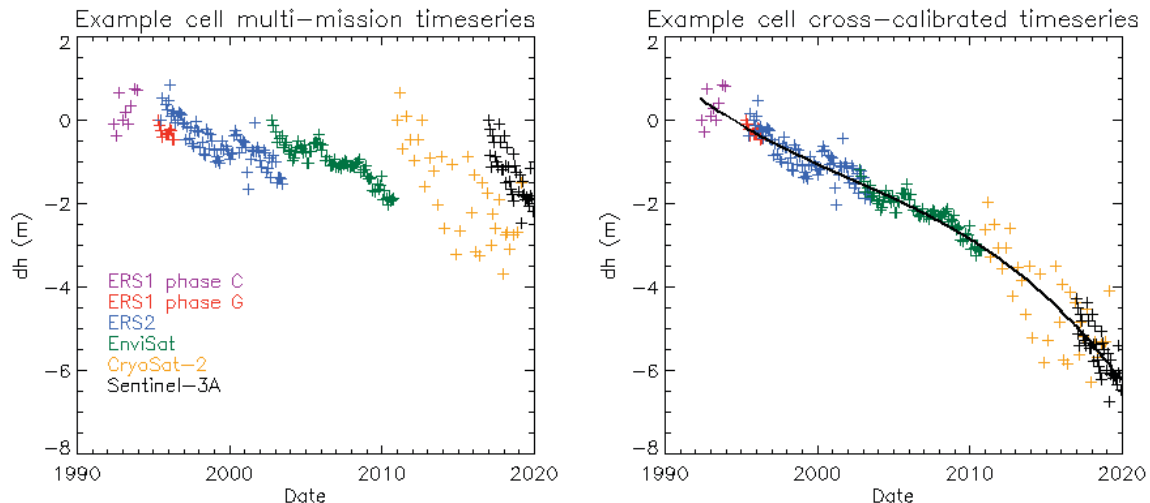

Fig. 3.1: Multi-mission time-series before (left) and after cross-calibration (right).

The regression algorithm returns the standard deviation of each term, given input uncertainty estimates. In this case the input uncertainties are the standard deviations of each data point in the time-series. Thus estimates of cross-calibration uncertainty can be obtained for each mission, assuming no error on the first.

This cross-calibration method has been chosen because it retains as much data as possible. Other methods cross-calibrate piecewise, between successive pairs of missions, often using only data from the start and end of the mission. In regions where data is sparse or one mission is missing these methods may be unusable. With the chosen method all of the data points in the time-series are used, and even if one mission is unrepresented in the time-series it is still possible to cross-calibrate the rest.

Mission data points are not inferred from the model. Biases are added to pre-existing data points only.

3.2.3.5 Surface elevation change rates

The surface elevation change time-series are used to derive surface elevation change rates by linear fitting to any required time period. The ground track spacing of most missions is wide compared to the ice dynamic variation on the ground, so single-cell time-series data is reported in preference to aggregated areas.

glaciers cci

Contract: 4000127593/19/I-NB
Algorithm Theoretical Basis
Document (ATBD)

Name: Glaciers_cci+D2.1_ATBD
Version: 1.0
Date: 10.10.2020
Page: 26

3.2.3.6 Error budget

There are three contributors to the uncertainty of the surface elevation change rate:
- input data
- cross-calibration
- modelling

The input data contribution depends on the distribution of elevation measurements within each grid cell/cycle. The standard deviation of these measurements does not formally account for all uncertainty sources, but will include residual errors from radar penetration and volume scattering that are not removed by retracking and backscatter power correction, and factors such as radar speckle, satellite location uncertainty and atmospheric attenuation uncertainty which decorrelate within the cycle period (Wingham et al, 1998). When calculating rates of surface elevation change, the input error component is formed from the individual errors on each data point used. It is taken as the root mean square of the input standard deviation, divided by the length of the time window.

The cross-calibration contribution accounts for errors in the biases calculated between missions. For a given period, data from one or more missions may be used. If only one mission is used then no cross-calibration is necessary and the cross-calibration uncertainty contribution is zero. If more missions are used then the root mean square of the cross-calibration uncertainties of the missions involved is converted to an uncertainty on the rate of change, by dividing by the time period over which the rate is calculated. The modelling contribution is the standard deviation of the model fit. This is also the measure of stability of the dataset. The three contributions are summed in quadrature to give a total uncertainty.

3.3 Seasonal dh/dt from ICESat in steep topography

3.3.1 Introduction

The increased spatial resolution and denser temporal coverage of ICESat-2 will likely lead to numerous, so far unrealistic glaciological applications, such as the large-area validation of DEMs (incl. determination of the TanDEM-X radar penetration mentioned under c) and the possibility to obtain glacier elevation changes with (sub-)seasonal temporal resolution. This would allow determining snow thickness on glaciers as well as detailed tracking of fast processes such as mass transfer by glacier surges.

ICESat-2 performance in extreme terrain, such as the Karakoram, will be compared to ICESat-1, especially regarding spatial density of information and representativeness of glacier elevation intervals, as well as to short term dh/dt trends from photogrammetry.

3.3.2 Methods

There are two possible methods for investigating ICESat-2 performance. Both will be evaluated;
- Surface modelling
- Crossovers

The results from both methods will be compared to ICESat-1 data processed in the same way, and to appropriate dh/dt datasets from other sources.

The surface modelling method is as described for the single-mission case in 3.2.2.1 above. Backscatter power correction is not necessary for laser altimeters, such as those on ICESat-1 and 2, and will not be implemented.

The crossover method calculates elevations at data points where ascending and descending orbit tracks cross. A time-series of elevation changes is built up by comparing each cycle of the mission to a reference cycle, which is selected for its good geographical coverage. ICESat-1 and 2 have 91-day cycles. The changes are gridded geographically and temporally, to produce cell-averaged time-series. Finally, correction for glacial isostatic adjustment is applied to each elevation in the resulting time-series.

Since the dataset required for this work is long-term and geographically averaged, only one of the six beams on ICESat-2 will be used. Use of all six reveals important small and short-term features, but is unnecessary on this scale.

The methodology used is very similar to that used for the seasonal and historic dh/dt investigations in Section 3.2.

3.3.3   Processing line

3.3.3.1   Regions of interest and grid projection

The main regions of interest are the Karakoram and Pamir mountains. These are covered in a single 5 km by 5 km grid, which uses the same projection as the NSIDC 8 m DEM mosaics from optical imagery (Shean 2017). The projection does not have an EPSG number, it is a custom Albers Equal-Area Conical projection, latitudes of true scale (standard parallels) 25° E, 47° N, central longitude (meridian) 85° E, central latitude 36°, ellipsoid WGS84.

Grid size 292 x 186, extreme bottom left at x = -1623 km, y = -225 km

3.3.3.2   Ingestion

The datasets to be used for validation over the Russian Arctic are used as the primary datasets in this investigation. They are ingested as described in 3.2.3.2 above, for the grid defined in 3.3.3.1. In this case backscatter power is retained for completeness only, as it will not be used.

Suitable datasets for comparison and validation will be identified once the extent of usable data produced by this project has been established.

3.3.3.3   Single-mission, single-cell surface elevation change time-series

For the surface modelling method, steps as described in 3.2.3.3 are followed, omitting the backscatter power correction step. For the crossover method, Fig. 3.2 shows the physical layout of a single crossover.
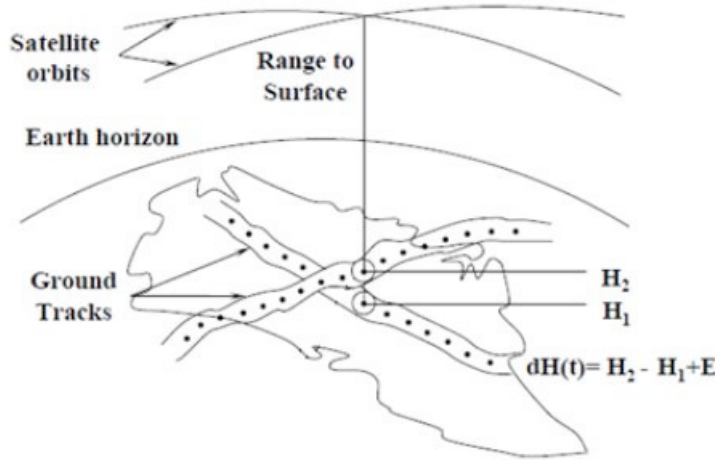
Fig. 3.2: Example crossover situation (taken from Nagler et al. 2018).

The radar altimeter measures the surface elevation at closely spaced discrete points along the satellite's ground track. In a small region around where an ascending and a descending track cross, an average height can be derived for each track, and this height will only be applicable to the very short overflight period. The difference between these heights is the change in surface elevation plus a random measurement error, which includes errors in the altimeter's height measurements and its orbital position, i.e.

$$dH(t) = H_2 - H_1 + E$$

where H_1 and H_2 are the heights at the crossover point and E is the measurement error.

There are several crossover methods available, but we use the dual crossover method (see Wingham et al. 1998) where one cycle of repeating tracks is used as reference, and height changes are derived at all crossovers between that cycle and each of the other cycles. This produces a time-series of height differences relative to the reference cycle height at each crossover.

$$\Delta h\left(x, t, t_{ref}\right) = \frac{1}{2}\left[\left(h_{At} - h_{D\,t_{ref}}\right) + \left(h_{At_{ref}} - h_{Dt}\right)\right]_{t=t_1\ldots t_N}$$

where h is height, At_{ref} and At are the ascending reference and comparison tracks respectively, and Dt_{ref} and Dt are the descending equivalents at the same crossover, x.

There may be several crossover locations in each regional grid cell. To regularise the time-series in each cell, the average Δh per cell per cycle-period is calculated. Filtering restricts the crossover locations used to those with a minimum number of nearby measurements (2 per pass), and where the numbers of measurements from ascending and descending passes are greater than a given ratio (0.5).

The standard deviation of the inputs to the averaged Δh is noted – this is the uncertainty from the input measurements, which will be used as a component of the total uncertainty of the product.

Contract: 4000127593/19/I-NB

Algorithm Theoretical Basis
Document (ATBD)

Name: Glaciers_cci+D2.1_ATBD
Version: 1.0
Date: 10.10.2020
Page: 29

More filtering is used to remove elevation change measurements that are excessively far from their main distribution. Values are removed if they amount to more than the annual change cycle magnitude plus the maximum change per annum for every year of time difference to the reference cycle. Time-series are removed if they contain less than 10 data points. Further filtering is based on a modelled fit to a seasonally cycling signal on an overall linear trend represented by:

$$dh = a0 + (a1 \times t) + a2 \, \sin((a3 \times 2\pi \times t) + a4)$$

where dh is change in elevation, t is time and a_0 to a_4 are constants.

If a time-series has a data point more than 3 standard deviations from the model fit, then that data point is rejected. As for the surface fitting method, the elevation change data is averaged over 30-day epochs. As for the surface fitting method, a correction for glacial isostatic uplift is applied to each data point, using the ICE-5G model (Peltier 2004).

3.3.3.4   Cross-calibration

Mission datasets are always treated separately, so no cross-calibration is required.

3.3.3.5   Surface elevation change rates

For both methods, these are calculated as in 3.2.3.5

3.3.3.6   Error budget

This is calculated in a similar way to 3.2.3.6, but is simpler as cross-calibration is not performed.

There are two contributors to the uncertainty of the surface elevation change rate:
- input data
- modelling

The input data contribution depends on the distribution of elevation measurements within each grid cell/cycle. The standard deviation of these measurements does not formally account for all uncertainty sources, but will include factors such as satellite location uncertainty and atmospheric attenuation uncertainty, which decorrelate within the cycle period (Wingham et al. 1998). When calculating rates of surface elevation change, the input error component is formed from the individual errors on each data point used. It is taken as the root mean square of the input standard deviation, divided by the length of the time window.

The modelling contribution is the standard deviation of the model fit. This is also the measure of stability of the dataset. The two contributions are summed in quadrature to give a total uncertainty.

Treichler and Kääb (2016) give a detailed performance and error analysis of ICESat-1 over small glaciers and rough topography, where many aspects will also apply to ICESat-2 data, and will be analysed in detail.

4. Velocity

4.1 Interferometric techniques

4.1.1 Introduction

To date, spaceborne methods for measuring ice velocity have largely focused on off-set/speckle tracking methods (OT) applied to optical and SAR sensors. These methods have been extensively applied to Greenland, Antarctica as well as glaciers and ice caps [RD-2] and have proven to be efficient for large-scale and continuous monitoring. However, SAR off-set/speckle tracking methods are amplitude-based and do not exploit the full information provided by SAR images. Therefore, the precision is mostly controlled by the spatial resolution of the sensor and reaches at best some meters/year. In contrast, differential SAR interferometry can reach a precision of one-two orders of magnitude better.

The use of SAR interferometry for ice velocity mapping over glaciers is often limited by temporal decorrelation and requires short time intervals. With a revised observation scenario with respect to the previous phase of CCI, the 6-day products of Sentinel-1 and the 14-day products of ALOS-2 PALSAR-2 are increasingly available in Arctic regions. We will test processing lines for ice velocity using InSAR along with offset-tracking and investigate the applicability for Arctic ice caps and glaciers with regard to the mapping of the flow fields of slow-moving glaciers and of the drainage divides of ice caps.

4.1.2 Method

SAR interferometry computes the phase delay between a pair of radar images acquired at different times for estimating the ground displacement over this time period. The interferometric phase delay is a sum of multiple contributions, namely the flat-earth phase, the topographic phase, the displacement phase, the atmospheric phase and the phase noise. For ice velocity mapping as well as for all other applications based on displacement mapping, the displacement phase must be isolated by subtracting all other contributions from the overall phase. In practice, flat-earth phase is modelled, topographic phase is estimated from an external DEM and atmospheric phase and phase noise are often neglected.

Because of the complex conjugation used for generating the phase, only the principal part of the phase is known, i.e. the phase ranges between $-\pi$ and π, and the phase must be unwrapped. Phase unwrapping is a complex procedure that may lead to large errors in phase measurements, e.g. in layover regions, shear zones, fast-flowing areas. Moreover, phase unwrapping only determines the relative value of the phase. The absolute phase is retrieved by matching the null phase with null displacement/velocity. The absolute phase is proportional to the displacement projected onto the observing line-of-sight.

When applied to glaciers and ice streams, SAR interferometry maps for each interferometric pair the ice velocity vector projected on the line-of-sight direction. If SAR acquisitions from at least two sufficiently different geometries (crossing orbits) are available over a region of interest, LOS velocity measurements can be used to compute the 2-D surface velocity vector field.

SAR interferometry on glaciers performs efficiently over areas with stable conditions over time: events such as melting, wind and snowfalls introduce additional phase delays and may lead to phase decorrelation. Although it is expected to reach a precision one to two orders of magnitude better than offset-tracking, InSAR is only applicable to slow-moving areas: meters per day velocities correspond to large displacements over a few days and cannot be measured by InSAR because they result into aliased fringes, which cannot be unwrapped (Fig. 4.1).
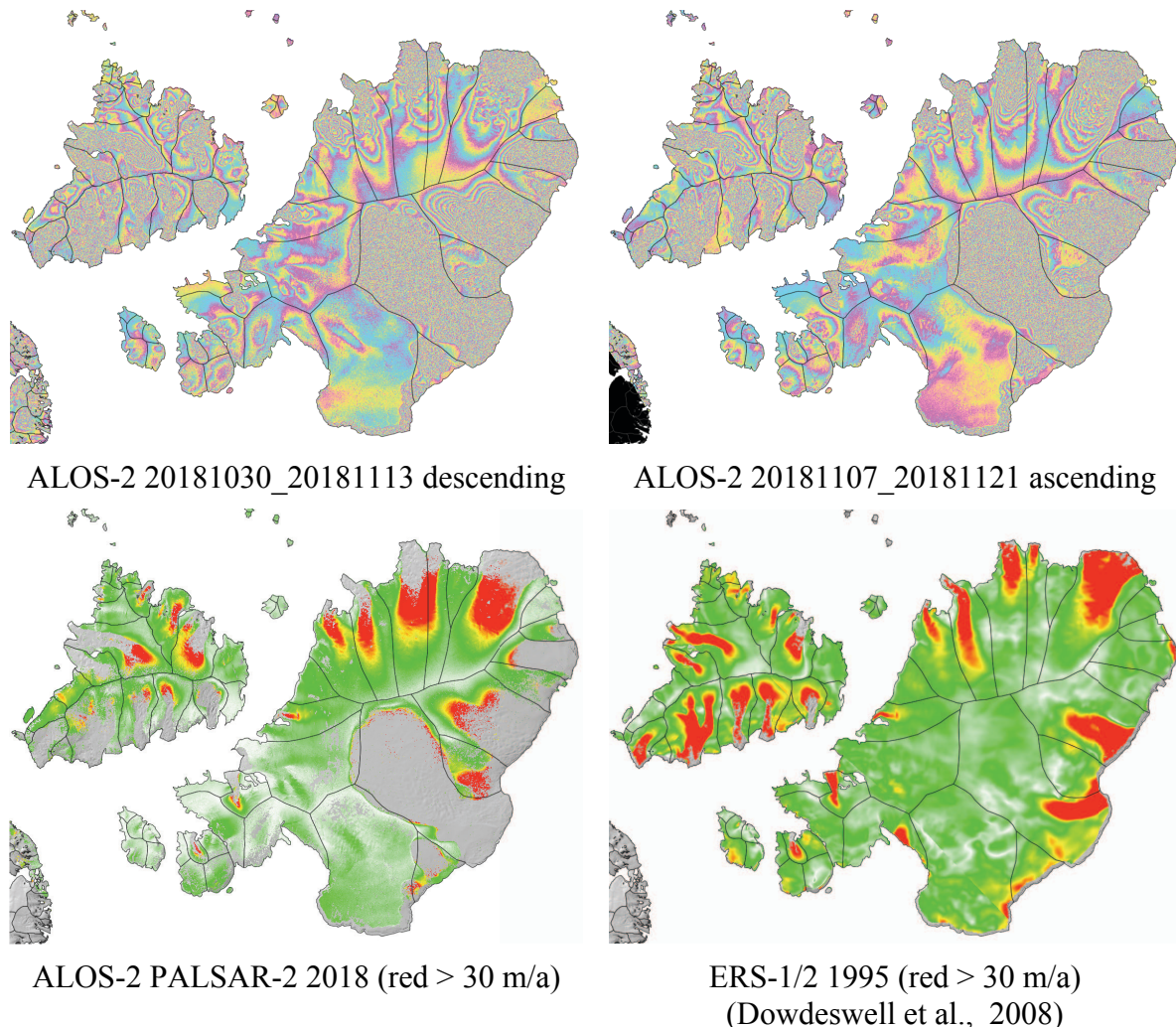

ALOS-2 20181030_20181113 descending   ALOS-2 20181107_20181121 ascending

ALOS-2 PALSAR-2 2018 (red > 30 m/a)   ERS-1/2 1995 (red > 30 m/a)
                                              (Dowdeswell et al., 2008)

Fig. 4.1: Examples for interferometric ice velocities. Upper row: wrapped ALOS-2 interferograms. Lower row: the related displacements.

4.1.3 Processing line

The proposed processing line is depicted in Fig. 4.2. Although this processing line is designed for Sentinel-1 TOPSAR acquisitions, it is straightforward to adapt it for other sensors or modes (e.g. Stripmap acquisitions mode). The interferometric processing consists of co-registration of SLC acquisitions at the burst level, generating a phase image and subtracting the flat earth and topographic phase contributions. The burst-wise processing yields wrapped displacement interferograms, which are mosaicked to obtain an area-wide interferogram. This is then unwrapped, the unwrapped phase is calibrated against slow-moving ground control points (GCPs) and subsequently converted into line-of-sight velocity.

Contract: 4000127593/19/I-NB
Algorithm Theoretical Basis
Document (ATBD)

Name: Glaciers_cci+D2.1_ATBD
Version: 1.0
Date: 10.10.2020
Page: 32

Because the antenna is sequentially steered from the aft to the fore in TOPSAR mode, phase jumps are introduced at the interferogram burst overlap whenever motion or co-registration error exists along the azimuth direction. These phase discontinuities may cause major errors during the phase unwrapping process, thus resulting in erroneous velocity. For this reason, a particular focus is set on the co-registration process: in order to reduce residual phase jumps, co-registration accounts for average local displacements between the master and slave acquisitions, using the ice velocity information from a multiannual offset-tracking velocity map.

Glaciers are often located in mountainous with complex topography and neighbouring ice-free terrain. This environment introduces layover and shadow areas in the SAR viewing geometry, which frequently introduce phase unwrapping errors. To mitigate such errors, areas corresponding to bedrock, layover and shadow are masked before phase unwrapping. If no fixed GCPs are available over the area of interest, the unwrapped phase is calibrated against a velocity template (e.g. multiannual ice velocity map from offset-tracking) using only slow-moving GCPs. Regions disconnected from each other are calibrated independently.

Interferometric processing is applied to all selected interferometric pairs and tracks (for Sentinel-1, 6-day pairs are used if available). The resulting LOS velocity maps are used for the inversion step, which is meant to retrieve the 2-D surface velocity field. Provided that velocity measurements from at least two different viewing geometries (i.e. two different heading angles) are available for a given point, the east-west (x) and north-south (y) velocity components can be determined.
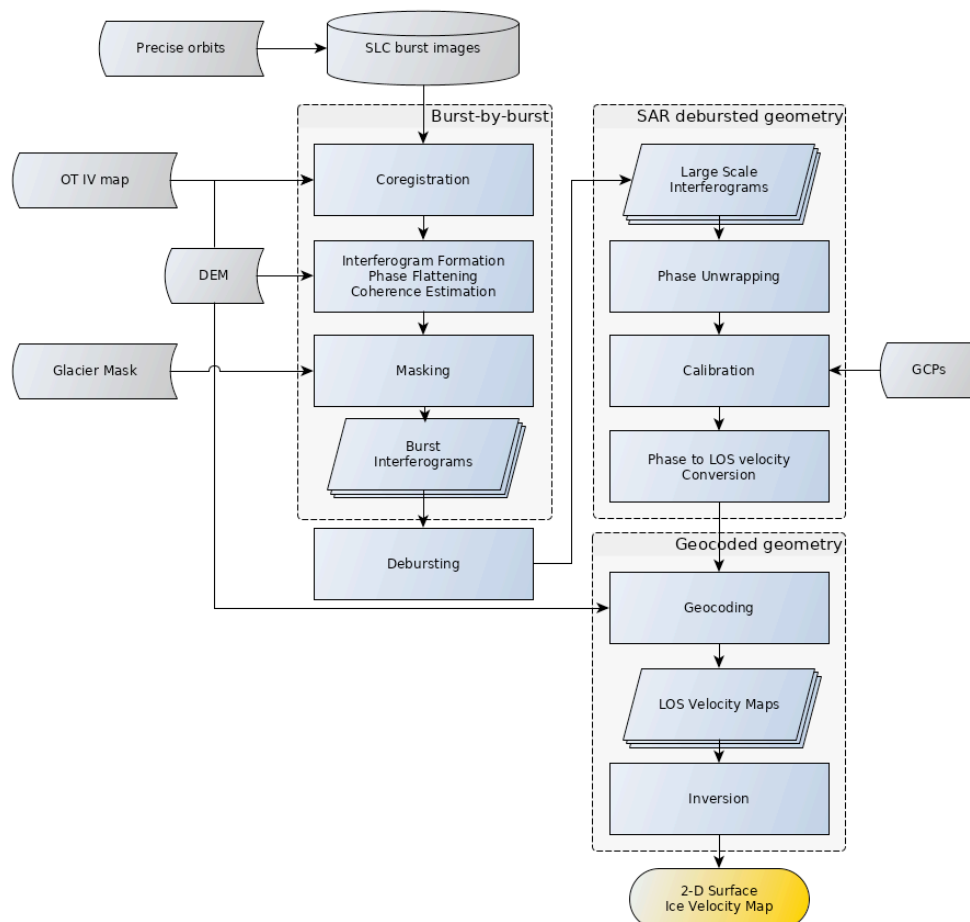

Fig. 4.2: SAR interferometry processing line for ice velocity retrieval.

4.2 Drainage divides from interferometry

4.2.1 Introduction

In order to split contiguous ice masses into individual glacier entities, digital drainage divides are required. Manual glacier separation by visual inspection of ice flow patterns is time-consuming and difficult. Semiautomatic algorithms that use a digital elevation model, outlines of glacier complexes, and hydro-logical modeling tools were proposed e.g. by Bolch et al. (2010), Kienholz et al. (2013) and Falaschi et al. (2017). A closer visual comparison of the derived extents of individual glaciers with the flow-velocities derived from SAR data often revealed important inconsistencies (Paul et al. 2015). Fringe patterns from wrapped differential SAR interferograms were thus proposed by Rastner et al. (2017) to manually correct the outlines of the drainage basins derived from semiautomatic algorithms, especially in terrain with low slope like the interior of ice caps. With the increasingly availability of coherent winter 6/12-day Sentinel-1 and 14-day ALOS-2 PALSAR-2 interferograms (see examples in Fig. 4.3 for part of Franz-Josef-Land), the use of fringe images to update drainage divides can be now applied to all major Arctic ice caps, with consistency tests across scene pairs.

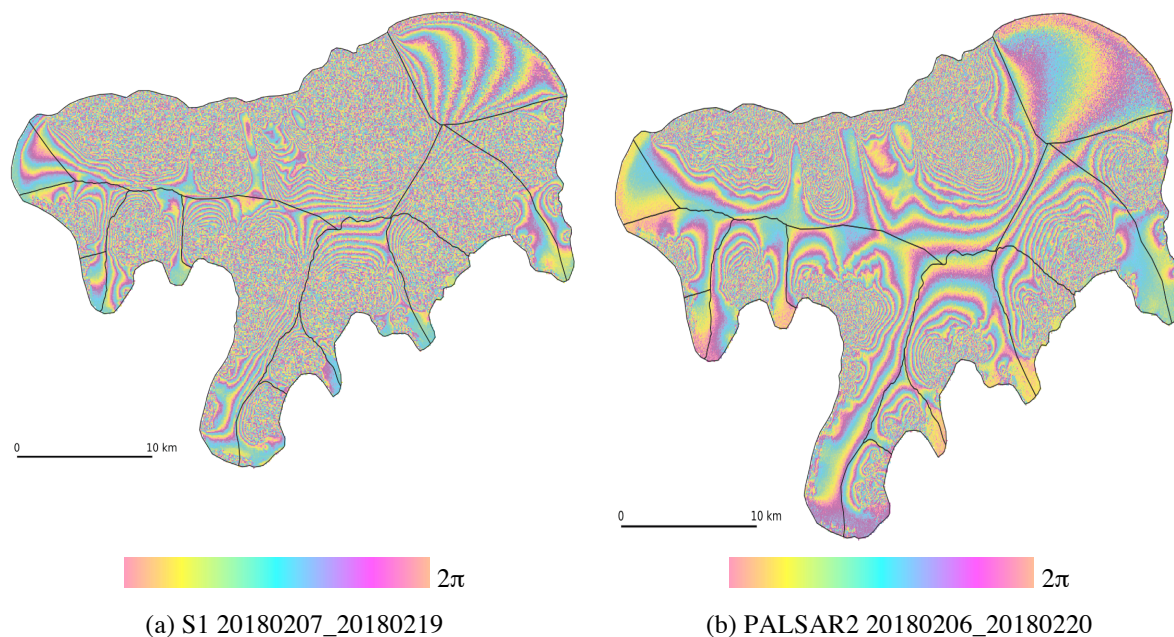(a) S1 20180207_20180219   (b) PALSAR2 20180206_20180220

Fig. 4.3: Sentinel-1 12-day differential interferogram from the 7th to the 19th of February 2018 (a) and ALOS-2 PALSAR-2 14-day differential interferogram from the 6th to the 20th of February 2018 (b) for part of Franz Josef Land. Ice divides are from RGI 5.0.

4.2.2 Methods

The principle of SAR interferometry is discussed in the previous section. The phase signals in differential SAR interferograms (i.e. the fringe images) can be interpreted as ice surface displacement in the satellite line-of-sight (LOS) direction with possible atmospheric disturbances. Whereas over Arctic areas the coherence is often low for the lower sections of the outlet glaciers because of fast ice flow, coherence is sufficiently high over the slower moving interior parts of the ice cap to obtain clearly visible fringes (see Fig. 4.3). Estimation and re-

moval of the topographic phase is performed using an external DEM, which should have an acquisition date that matches that of the SAR dataset close enough to not expect any major topographic signal left on the differential interferograms. However, because the perpendicular baseline of the current Sentinel-1 and ALOS-2 PALSAR-2 image pairs is generally below 100 m, the sensitivity of these sensors to topographic errors is very limited. If the outlines of the drainage basins derived from the DEM do not follow the fringe patterns, they are manually edited to the extent possible.

4.2.3   Processing line

InSAR, see previous section but without phase unwrapping.

4.3   Mitigation of ionospheric-induced azimuth shifts

4.3.1   Introduction

In polar regions, the measurement of the azimuth offset-field is often corrupted by spurious shifts induced by ionospheric variations, in particular at L-band (e.g. Strozzi et al. 2008). In the example of Fig. 4.4, refering to a 14-day ALOS-2 PALSAR-2 image pair around Kronebreen (Svalbard), errors of about +/-2 m in 14 days are visible in the azimuth offset-field as elongated stripes crossing the image in nearly the range (horizontal) direction.

±8 m   ±8 m
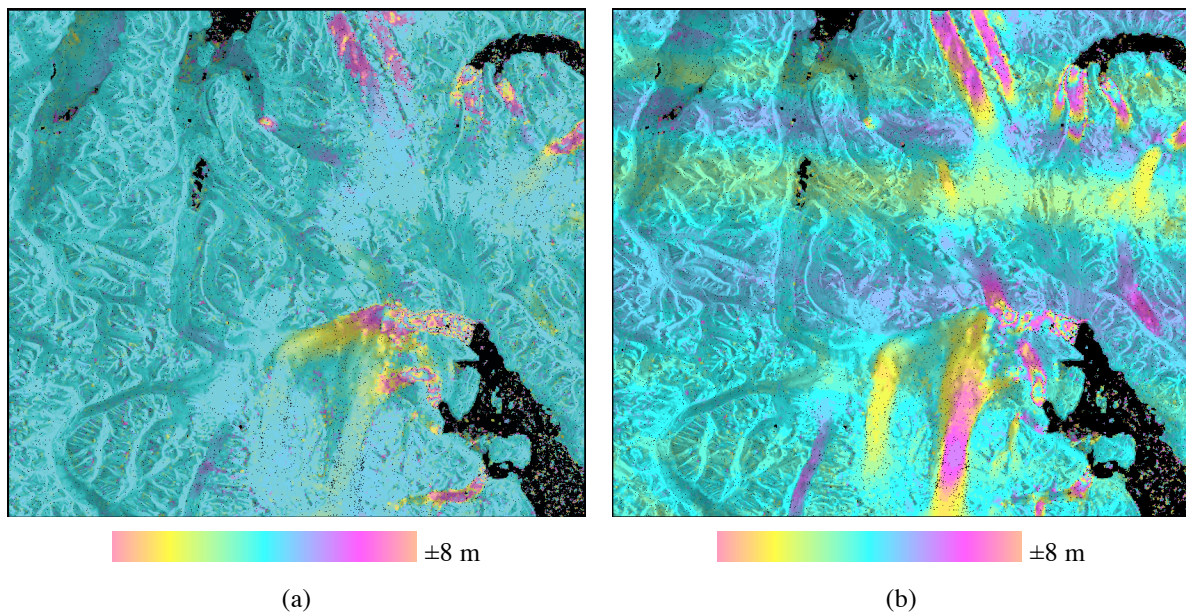
(a)   (b)

Fig. 4.4: Range (a) and azimuth (b) offset fields for the ALOS-2 PALSAR-2 image pair acquired between 11. and 25. February 2019 with an acquisition time interval of 14 days.

4.3.2   Methods

Range split-spectrum technique
The first idea to correct for the azimuth shifts is to use the range split-spectrum technique, which has proven very effective to remove ionospheric phase screens for differential SAR interferograms (Gomba et al. 2016). The azimuth shifts are indeed proportional to the first azimuth derivative of the ionospheric phase screen. However, as indicated by De Zan and Gomba (2019), the split-spectrum technique can only correct large-scale components of the ionospheric disturbance, because the sensitivity of the double difference interferogram to ion-

glaciers cci

Contract: 4000127593/19/I-NB
Algorithm Theoretical Basis
Document (ATBD)

Name: Glaciers_cci+D2.1_ATBD
Version: 1.0
Date: 10.10.2020
Page: 35

ospheric variations is much lower than that of the azimuth offset-field. In the example of Fig. 4.5 only a large scale phase gradient can be observed along the northwest-southeast direction, but no streaking in the range direction is detected with the interferometric phase.

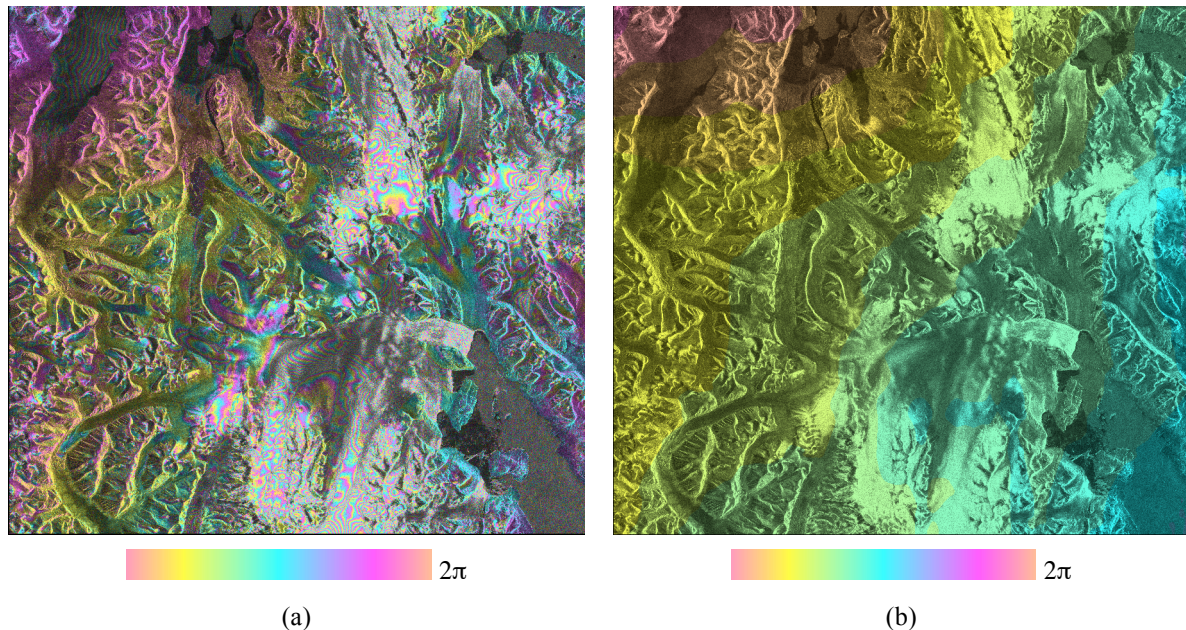(a)   (b)

Fig. 4.5: (a) Differential ALOS-2 PALSAR-2 interferogram between the 11. and the 25. of February 2019. (b) Ionospheric phase compensation exploiting the range split-spectrum technique.

Azimuth split-beam technique

In order to estimate finer scale spatial variations, De Zan and Gomba (2019) proposed to exploit the difference between the azimuth shifts calculated for a lower and an upper sub-band of the azimuth bandwidth (i.e. the differential shifts). The two shifts are identical for a physical shift on the ground and will cancel out in the difference, but they will differ in case of ionospheric oscillations. In particular, the shift difference corresponds to the second azimuth derivative of the ionospheric phase screen. Considering that the azimuth shifts reflect the first derivative of the phase screen, the correct operator to retrieve the azimuth shifts from the differential shifts is an integrator in azimuth direction. Figure 4.6 (a) shows the differential shifts for the 14-day ALOS-2 PALSAR-2 image pair around Kronebreen. It is clear that the differential shifts are rather noisy and an averaging step is needed. De Zan and Gomba (2019) proposed to solve the issue of determining the right integration operator and spatial averaging in one step, with the use of a prediction error filter. Figures 4.6 (b) shows the finally estimated azimuth shifts and Fig. 4.6 (c) the residual shifts, which should contain only ground motion plus components of the ionospheric disturbances that the filter was not able to estimate correctly.
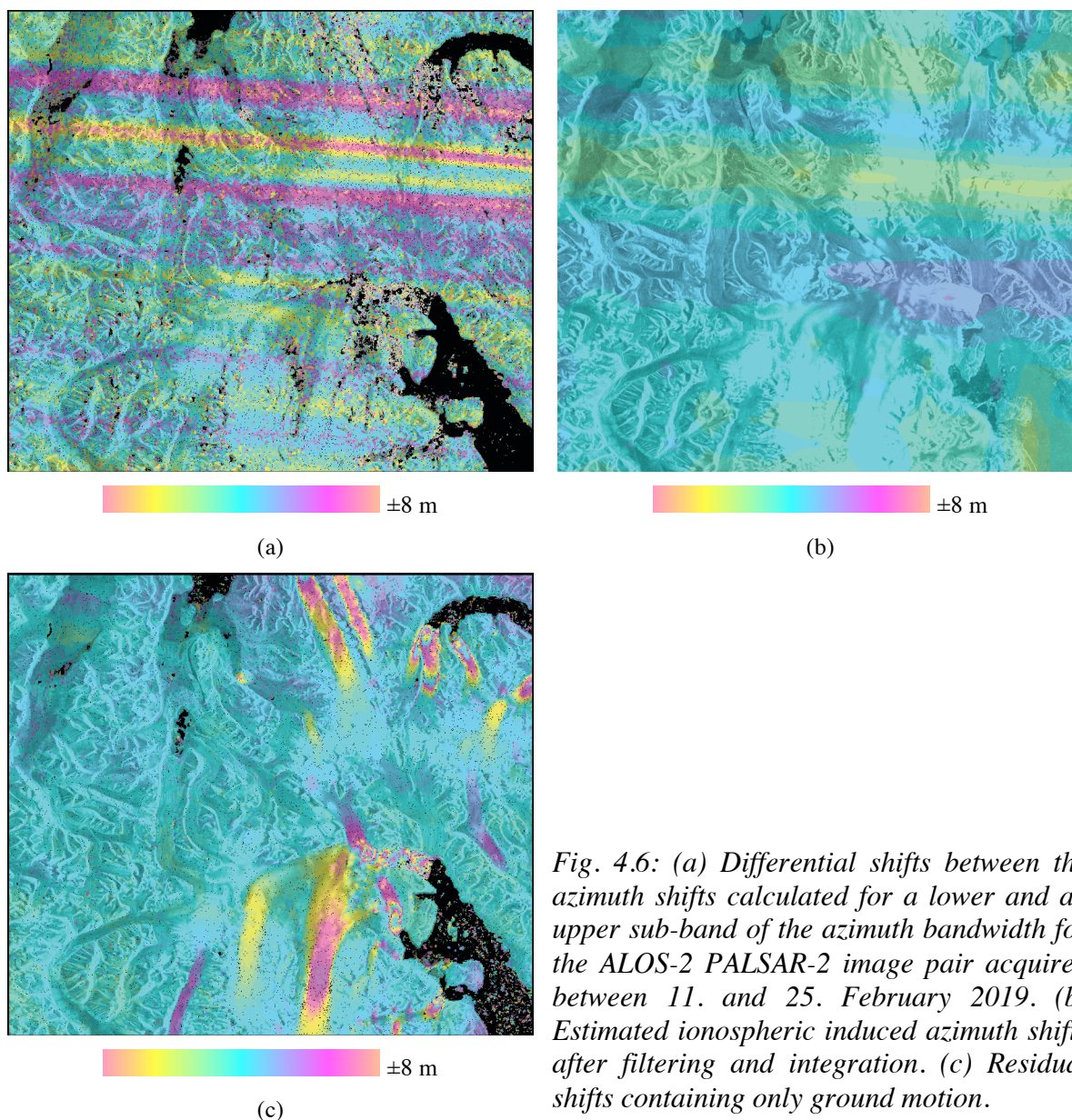
(a)

(b)

(c)

Fig. 4.6: (a) Differential shifts between the azimuth shifts calculated for a lower and an upper sub-band of the azimuth bandwidth for the ALOS-2 PALSAR-2 image pair acquired between 11. and 25. February 2019. (b) Estimated ionospheric induced azimuth shifts after filtering and integration. (c) Residual shifts containing only ground motion.

High-pass filter along the range direction

Ionospheric anomalies are clearly visible in the azimuth offset field but hardly visible in the range offset field (Fig. 4.4). Furthermore, the typical azimuth streaking geometry of ionospheric azimuth offsets differs from the more localized motion fields of glaciers. In order to estimate the ionospheric part of the azimuth offsets, Wegmüller et al. (2006) proposed to first reject azimuth offset estimates for areas with significant range offsets. Furthermore, estimates over specific areas of interest (e.g. large glaciers) are rejected (Fig. 4.7 (a)). Then, the remaining azimuth offset field is filtered and interpolated taking into account the strong directionality of the azimuth streaks by using filters and interpolators that are significantly longer in the range direction than in the azimuth direction (Fig. 4.7 (b)). Finally, this ionospheric azimuth offset estimate is subtracted from the initial offset field and the remaining_offsets are interpreted as ground surface movements (Fig. 4.7 (c)).
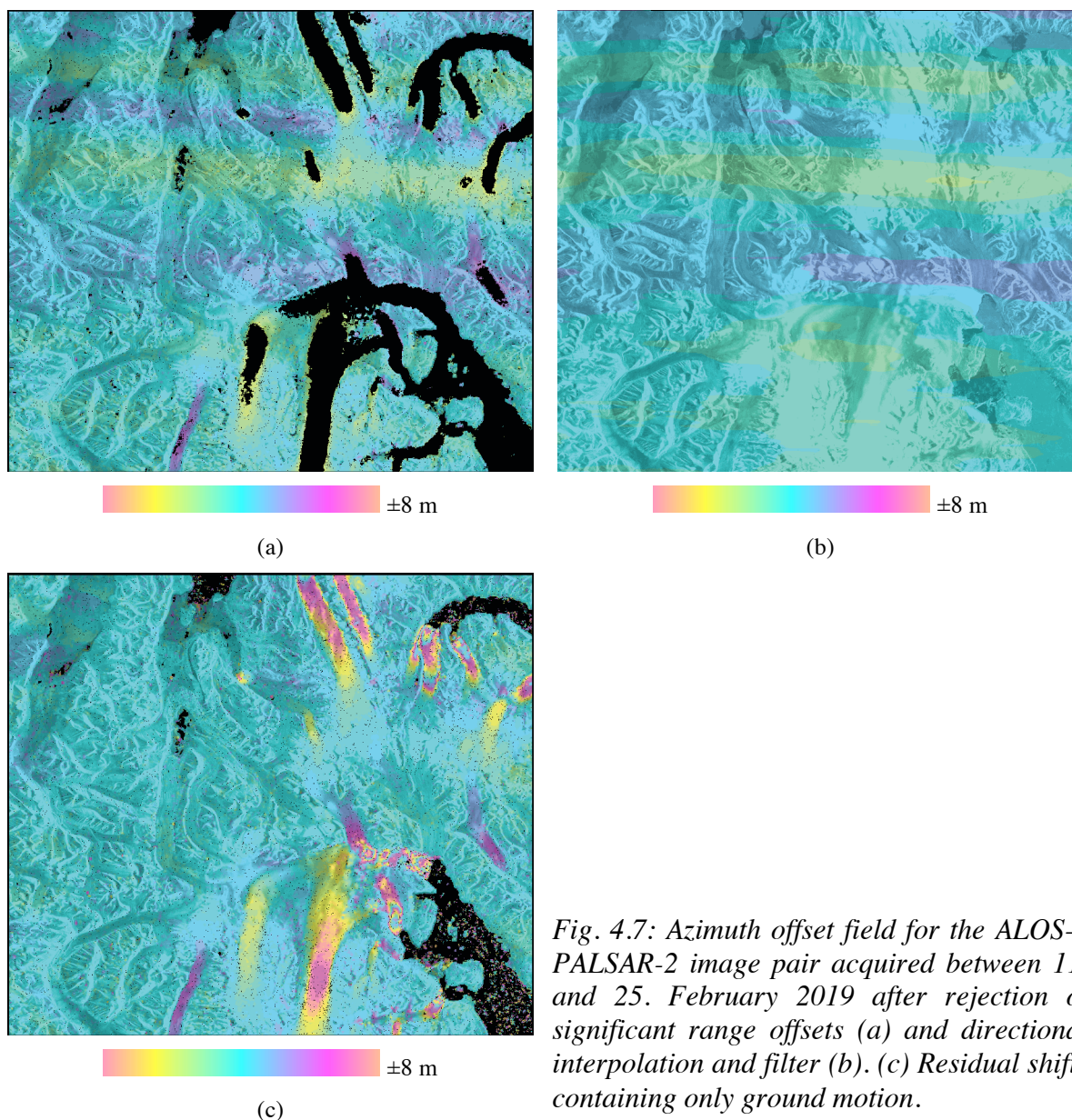
(a)

(b)

(c)

Fig. 4.7: Azimuth offset field for the ALOS-2 PALSAR-2 image pair acquired between 11. and 25. February 2019 after rejection of significant range offsets (a) and directional interpolation and filter (b). (c) Residual shifts containing only ground motion.

4.3.3 Processing line

The correction of the azimuth shifts using the range split-spectrum technique is effective only for large scale components of the ionospheric disturbance, but cannot account for the higher frequency streaking in the range direction and is therefore not considered in the operational processing lines. The most critical steps of the azimuth split-beam technique are the determination of the right integration operator and the spatial averaging, which could be operationally solved with the use of a prediction error filter. The most critical steps of the technique exploiting a high-pass filter along the range direction are the selection of the threshold for the rejection of significant range offsets and the directional filtering and interpolation. Considering that a similar performance of the azimuth split-beam technique and of the technique exploiting a high-pass filter along the range direction can be obtained (Figures 4.6 (c) and Fig. 4.7 (c)) and our long experience using the latter method, we will implement also in future processing the correction based on the high-pass filter along the range direction. In Fig. 4.8 the principle processing line for the mitigation of ionospheric-induced azimuth shifts is shown.
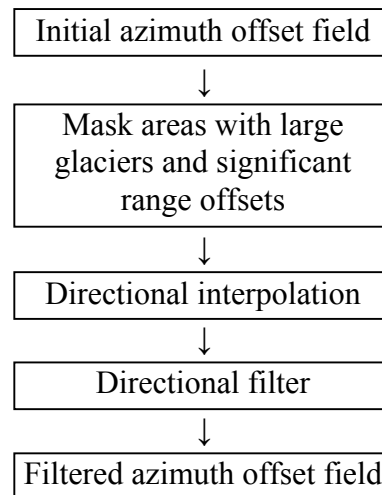
```
┌─────────────────────────────────┐
│   Initial azimuth offset field  │
└─────────────────────────────────┘
                 ↓
┌─────────────────────────────────┐
│      Mask areas with large      │
│    glaciers and significant     │
│          range offsets          │
└─────────────────────────────────┘
                 ↓
┌─────────────────────────────────┐
│     Directional interpolation   │
└─────────────────────────────────┘
                 ↓
┌─────────────────────────────────┐
│        Directional filter       │
└─────────────────────────────────┘
                 ↓
┌─────────────────────────────────┐
│   Filtered azimuth offset field │
└─────────────────────────────────┘
```

Fig. 4.8: Generalized processing line for the mitigation of ionospheric-induced azimuth shifts.

4.4 Historical time series over Arctic regions

4.4.1 Introduction

The computation of circum-Arctic surface velocity maps of glaciers and ice caps is operational with the Sentinel-1 constellation every 12 days since 2015, revealing new insights in glacier dynamics (e.g. Strozzi et al. 2017b). For a comparison of recent glacier's behaviour of polar regions with the situation in the nineteen-nineties, the JERS-1 SAR data archives (1994-1998) at JAXA and ESA were recently made available to the public free of charge. In addition, ERS-1 SAR of the 1991 and 1994 ice missions with repeat intervals of multiple of 3 days can complement the JERS-1 data coverage over Svalbard and the Russian Arctic, which is not exhaustive everywhere.

4.4.2 Methods

JERS-1 and ERS-1 SAR images are processed with offset-tracking procedures (e.g. Strozzi et al. 2002) to three-dimensional ice surface displacement maps combining the slant-range and azimuth offsets by assuming that flow occurs parallel to the ice surface as estimated from the DEM. The offset-tracking processing lines available from the previous phases of the project are adapted to the format of the recently released data at ESRIN and JAXA. Ice surface velocity maps in the nineteen-nineties from JERS-1 and ERS-1 can be thus compared to recent results from Sentinel-1 (see examples Figs. 4.9 and 4.10).

Processing line

In Fig. 4.11 the principle processing line for offset-tracking of JERS-1 and ERS-1 data is presented. While the JERS-1 SAR data from ESA (https://tpm-ds.eo.esa.int/oads/access/ collection/JERS1-SLC) are distributed in SLC (Level 1) format, those from JAXA (gportal.jaxa.jp) are distributed in RAW (Level 0) format.

Contract: 4000127593/19/I-NB

Algorithm Theoretical Basis
Document (ATBD)

Name: Glaciers_cci+D2.1_ATBD
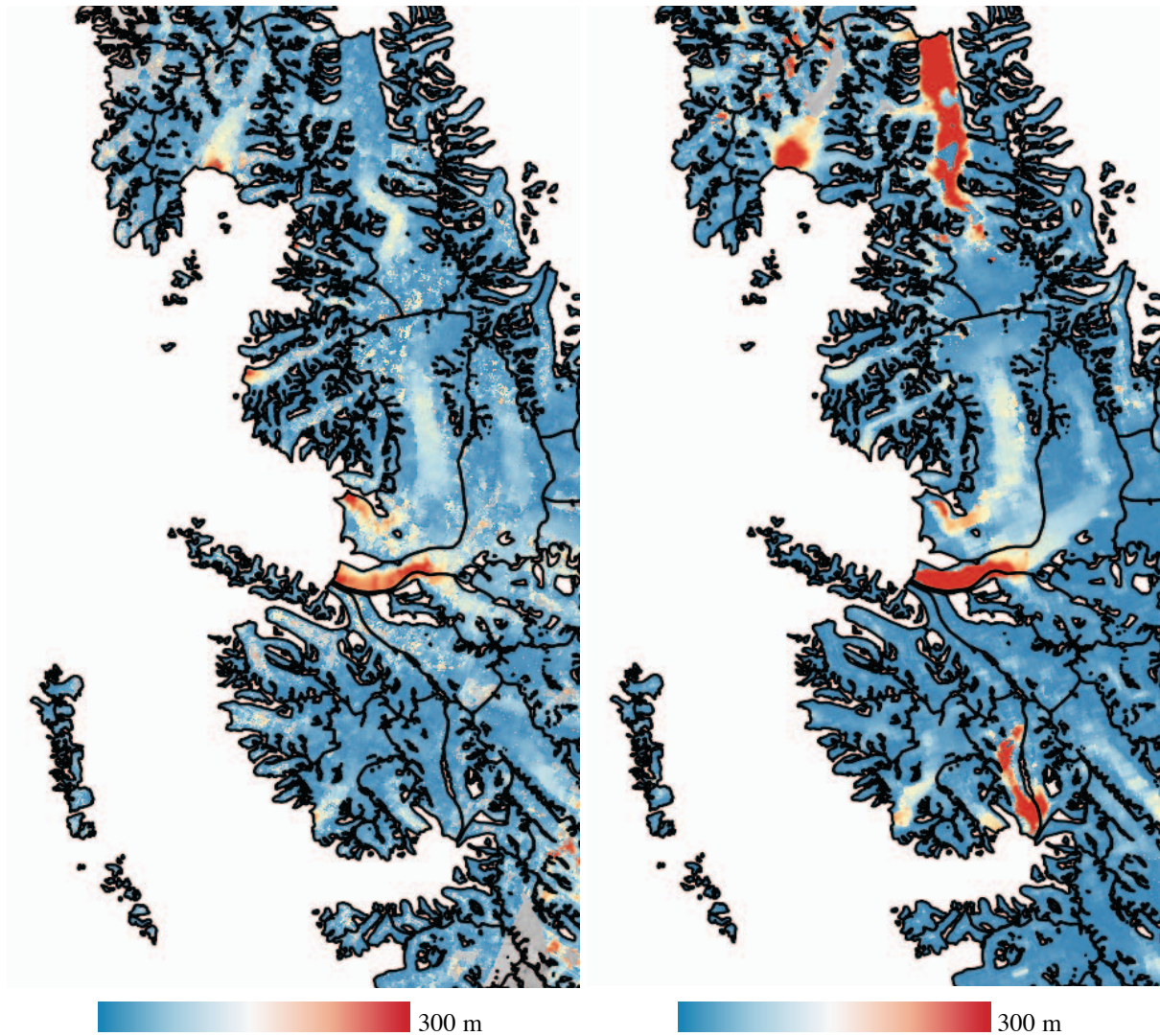Version: 1.0
Date: 10.10.2020
Page: 39

Fig. 4.9: Ice velocity maps for part of the Svalbard Archipelago from JERS-1 (left) and Sentinel-1 (right).
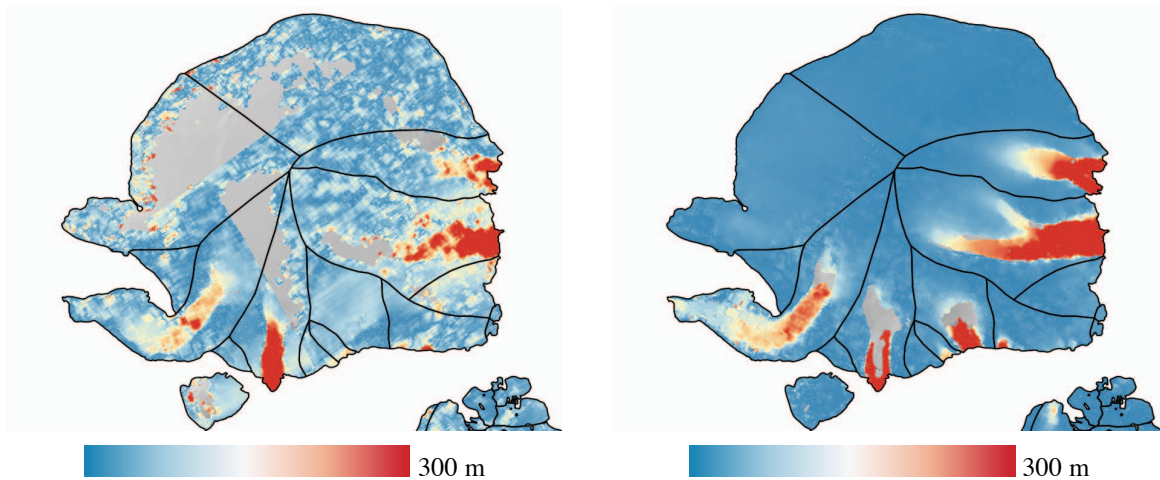

Fig. 4.10: Ice velocity maps for part of Severnaya Zemlya from ERS-1 (left) and Sentinel-1 (right).
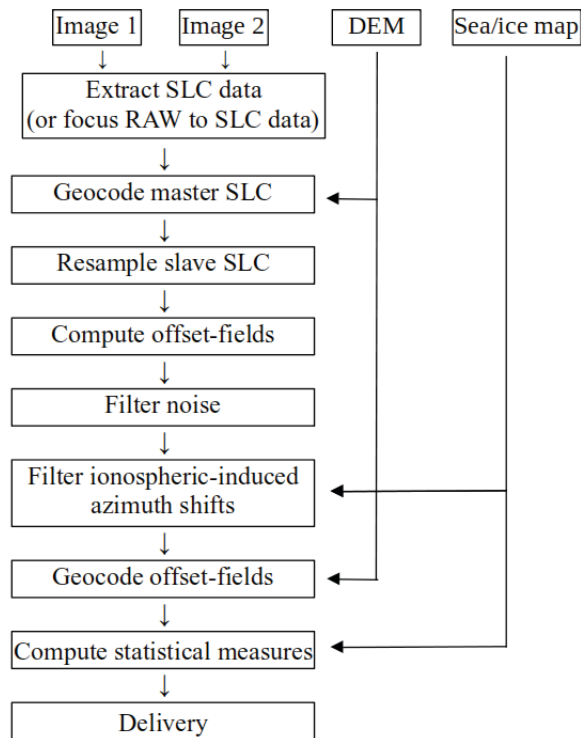
Fig. 4.11: Generalized processing line for offset-tracking of JERS-1 and ERS-1 data.

4.5 Sensor and method synergies

4.5.1 Introduction

Surging glaciers can flow very fast (>10 m/day) and velocities tend to be spatially and temporarily highly variable (e.g. Paul et al. 2017b, Strozzi et al. 2017b and references cited above). We will develop methods for the synergetic use of optical (e.g. Landsat, ASTER, Sentinel-2) and SAR (e.g. JERS-1, TerraSAR-X, Sentinel-1) sensors to increase the temporal density of velocity data to reduce data gaps and increase the reliability of the products. Time series processing might also benefit from new approaches such as stack and cloud processing and further improvement of automated methods for bias detection and accuracy improvement.

Besides, as described in section 4.1, SAR interferometry requires data from crossing orbits (e.g. ascending and descending) to derive ice velocity, but some glaciers are only covered by a single track of Sentinel-1. As a consequence, InSAR cannot always provide a comprehensive coverage of ice flow in glacier areas. Since offset-tracking can efficiently retrieve both horizontal velocity components from a single geometry, although with a coarser accuracy than InSAR, we develop a synergistic use of offset-tracking and SAR interferometry in order to improve the overall coverage of the ice velocity products over Arctic glaciers and ice caps.

4.5.2 Methods

Merging InSAR with OT flow direction
Sentinel-1 has significantly increased SAR coverage in the Arctic, with routine 6- and 12-day coverage of Greenland margins and peripheral glaciers as well as smaller Arctic ice caps and glaciers. Nevertheless, some glacier areas are covered by only one single Sentinel-1 track,

Contract: 4000127593/19/I-NB
Algorithm Theoretical Basis
Document (ATBD)

Name: Glaciers_cci+D2.1_ATBD
Version: 1.0
Date: 10.10.2020
Page: 41

making it impossible to derive the ice velocity vector from InSAR only and reducing the applicability of InSAR for ice velocity retrieval. However, if the flow direction is known and assumed constant, InSAR measurements can be used to retrieve the magnitude of the velocity vector. In contrast to InSAR, offset-tracking (OT) can derive velocity vector components from a single acquisition geometry. Even though OT is much less accurate than InSAR when applied to a single pair of images, it reaches a satisfactory accuracy when stacking measurements over longer periods. To improve existing maps and maximize the synergy of InSAR and OT, we combine the flow direction derived from OT with the InSAR line-of-sight velocity measurements, assuming stability of the flowlines over time. With this approach, the velocity field can be determined, wherever single- or multi-track InSAR measurements are available, except on the ice divide where the flow vector is null.

4.5.3 Processing line

The combined approach of InSAR and OT flow direction is described in Fig. 4.12. In this flowchart, the InSAR processing corresponds to the interferometric processing for ice velocity retrieval described in Section 4.1.3. In parallel to the interferometric processing, the flow direction is derived from the OT multiannual velocity map. The flow direction is computed as the angle between the velocity vector and the east direction.

The line-of-sight (LOS) velocity maps resulting from the interferometric processing and the flow direction map are combined in the inversion process, which consists of a weighted least squares linear regression. Since the LOS velocity data points are the projected measurements of the velocity vector, they have a linear dependence on the projection coefficients and this linear dependence has a slope corresponding to the velocity magnitude. The projection coefficients are defined by the flow direction and the InSAR geometry (incidence and heading angles). Therefore, the inversion process enables estimating the velocity magnitude, which is finally projected on the x and y direction of the ice flow for computing the x-, y- and z-components of the velocity field.
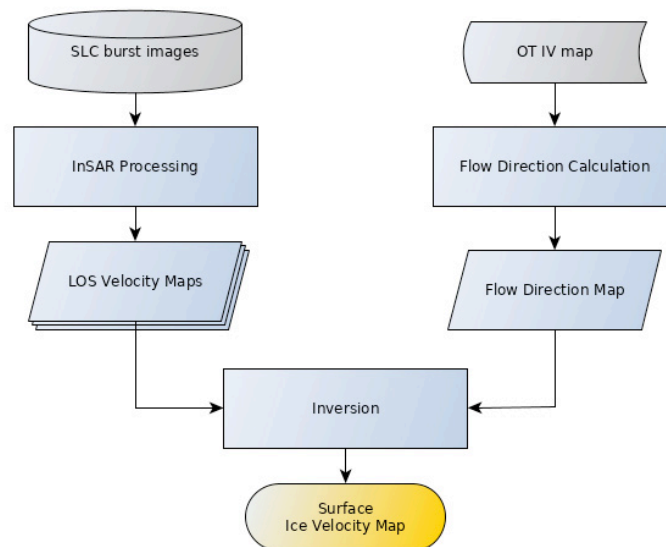

Fig. 4.12: Combined approach of SAR interferometry and offset-tracking for ice velocity retrieval.

5. References

Atwood, D., Meyer, F. and Arendt, A. (2010): Using L-band SAR coherence to delineate glacier extent. *Canadian Journal of Remote Sensing*, 36, S186-S195.

Bolch T., Menounos, B. and Wheate, R. (2010): Landsat-based inventory of glaciers in western Canada, 1985–2005. *Remote Sensing of Environ*ment, 114:127-137.

De Zan, F. and Gomba, G. (2019) : Correction of Ionospheric-induced Azimuth Shifts in Coherent SAR Pairs: Split Spectrum and Differential Shifts, Proceedings of the ESA Living Planet Symposium, Milano (Italy), 13-17 May 2019.

Dehecq, A., Millan, R., Berthier, E., Gourmelen, N., Trouvé, E. and Vionnet, V. (2016): Elevation changes inferred from TanDEM-X data over the Mont-Blanc area: Impact of the X-band interferometric bias. *IEEE Journal of Selected Topics in Applied Earth Observations and Remote Sensing*, 9 (8), 3870–3882.

Dowdeswell, J.A. and Williams, M. (1997): Surge-type glaciers in the Russian High Arctic identified from digital satellite imagery. *Journal of Glaciology*, 43(145), 489–494.

Dowdeswell, J., Hodgkins, R., Nutall, A., Hagen, J.-O. and Hamilton, G. (1995): Mass-balance change as a control on the frequency and occurrence of glacier surges in Svalbard and Norwegian High Arctic. *Geophysical Research Letters*, 22, 2909–2912.

Dowdeswell J., Benham, T., Strozzi, T. and Hagen, J.O. (2008) : Iceberg calving flux and mass balance of the Austfonna ice cap on Nordaustlandet, Svalbard. *Journal of Geophysical Research*, 113, F03022, doi: 10.1029/2007JF000905

Falaschi D., Bolch, T., Rastner, P., Lenzano, M.G., Lenzano, L., Lo Vecchio, A. and Moragues, S. (2017) : Mass changes of alpine glaciers at the eastern margin of the Northern and Southern Patagonian Icefields between 2000 and 2012. *Journal of Glaciology*, 33(238) 258–272.

Foresta, L., Gourmelen, N., Pálsson, F., Nienow, P., Björnsson, H. and Shepherd, A. (2016): Surface elevation change and mass balance of Icelandic ice caps derived from swath mode CryoSat-2 altimetry. *Geophysical Research Letters*, 43 (12), 138-145.

Frey, H., Paul, F. and Strozzi, T. (2012): Compilation of a glacier inventory for the western Himalayas from satellite data: Methods, challenges and results. *Remote Sensing of Environment*, 124, 832-843.

Gardelle, J., Berthier, E. and Arnaud, Y. (2012): Slight mass gain of Karakoram glaciers in the early twenty-first century. *Nature Geoscience*. 5(5), 322-325.

Goerlich, F., Bolch, T., Mukherjee, K. and Pieczonka, T. (2017): Glacier mass loss during the 1960s and 1970s in the Ak-Shirak range (Kyrgyzstan) from multiple stereoscopic Corona and Hexagon imagery. *Remote Sensing*, 9(3), 275; doi:10.3390/rs9030275.

Gomba, G., Parizzi, A., De Zan, F., Eineder, M. and Bamler, R. (2016) : Toward operational compensation of ionospheric effects in SAR Interferograms: The Split-Spectrum Method, *IEEE Transactions on Geoscience and Remote Sensing*, 54(3), 1446-1461.

Haga, O., McNabb, R., Nuth, C., Altena, B., Schellenberger, T. and Kääb, A. (2020): From high friction zone to frontal collapse: Dynamics of an ongoing tidewater glacier surge, Negribreen, Svalbard. *Journal of Glaciology*, 1-13. doi:10.1017/jog.2020.43.

Haeberli, W., Huggel, C., Paul, F. and Zemp, M. (2020): The response of glaciers to climate change: Observations and impacts In: Shroder, J. (Editor in Chief), James, L.A., Harden, C.P., Clague, J.J. (Eds.): Treatise on Geomorphology. Academic Press, San Diego, CA, vol. 13, Geomorphology of Human Disturbances, Climate Change, and Natural Hazards.

Harrison, W.D., Osipova, G.B., Nosenko, G.A., Espizua, L., Kääb, A., Fischer, L., Huggel, C., Craw Burns, P.A., Truffer, M. and Lai, A.W. (2015): *Glacier Surges*. In: W. Haeberli and C. Whitemann (Eds.), Snow and Ice-related Hazards, Risks, and Disasters. Elsevier, Amsterdam, 437-485.

Herreid, S. and Truffer, M. (2016): Automated detection of unstable glacier flow and a spectrum of speedup behavior in the Alaska Range. *Journal of Geophysical Research*, 121, 64–81, doi:10.1002/2015JF003502.

Holzer, N., Vijay, S., Yao, T., Xu, B., Buchroithner, M. and Bolch, T. (2015): Four decades of glacier variations at Muztagh Ata (eastern Pamir): a multi-sensor study including Hexagon KH-9 and Pléiades *data. The Cryosphere*, 9(6), 2071-2088.

Kääb, A., Berthier, E., Nuth, C., Gardelle, J. and Arnaud, Y. (2012): Contrasting patterns of early twenty-first-century glacier mass change in the Himalayas. *Nature*, 488(7412), 495–498.

Kääb, A., Winsvold S.H., Altena B, Nuth C., Nagler T., Wuite J. (2016): Glacier remote sensing using Sentinel-2. Part I: Radiometric and geometric performance, and application to ice velocity. *Remote Sensing*, 8(7), 598; 8; doi:10.3390/rs8070598.

Kienholz, C., Hock, R. and Arendt, A.A. (2013): A new semi-automatic approach for dividing glacier complexes into individual glaciers. *Journal of Glaciology*, 59(217), 913-925.

Lippl, S., Vijay, S. and Braun, M. (2018): Automatic delineation of debris-covered glaciers using InSAR coherence derived from X-, C-and L-band radar data: a case study of Yazgyl Glacier. *Journal of Glaciology*, 64 (247): 811-821.

Maurer, J. and Rupper, S. (2015): Tapping into the Hexagon spy imagery database: A new automated pipeline for geomorphic change detection. *ISPRS Journal of Photogrammetry and Remote Sensing*, 108, 113–127

Maurer, J.M., Schaefer, J.M., Rupper, S.B. and Corley, A. (2019): Acceleration of ice loss across the Himalayas over the past 40 years. *Science Advances*, 5, eaav7266.

McNabb, R., Nuth, C., Kääb, A. and Girod, L. (2019): Sensitivity of geodetic glacier mass balance estimation to DEM void interpolation. *The Cryosphere*, 13, 895–910.

Mölg, N., Bolch, T., Rastner, P., Strozzi, T. and Paul, F. (2018): A consistent glacier inventory for the Karakoram and Pamir region derived from Landsat data: Distribution of debris cover and mapping challenges. *Earth Systems Science Data*, 10, 1807-1827.

Nagler, T. et al. (2018): Algorithm Theoretical Baseline Document (ATBD) for the Antarctic Ice Sheet CCI Project of ESA's Climate Change Initiative, version 3.0. Available from http://www.esa-icesheets-antarctica-cci.org/

Nuth, C. and Kääb, A. (2011): Co-registration and bias corrections of satellite elevation data sets for quantifying glacier thickness change. *The Cryosphere*, 5, 271-290

Paul, F. (2015): Revealing glacier flow and surge dynamics from animated satellite image sequences: Examples from the Karakoram. *The Cryosphere*, 9, 2201-2214.

Paul, F., Huggel, C. and Kääb, A. (2004): Combining satellite multispectral image data and a digital elevation model for mapping of debris-covered glaciers. *Remote Sensing of Environment*, 89 (4), 510-518.

Paul F., Bolch, T., Kääb, A., Nagler, T., Nuth, C., Scharrer, K., Shepherd, A., Strozzi, T., Ticconi, F., Bhambri, R., et al. (2015) : The glaciers climate change initiative: Methods for creating glacier area, elevation change and velocity products. *Remote Sensing of Environment*, 113:1-19.

Paul, F., Winsvold, S.H., Kääb, A., Nagler, T. and Schwaizer, G. (2016): Glacier Remote Sensing Using Sentinel-2. Part II: Mapping glacier extents and surface facies, and comparison to Landsat 8. *Remote Sensing*, 8(7), 575; doi:10.3390/rs8070575.

Contract: 4000127593/19/I-NB
Algorithm Theoretical Basis
Document (ATBD)

Name: Glaciers_cci+D2.1_ATBD
Version: 1.0
Date: 10.10.2020
Page: 44

Paul, F., Bolch, T., Briggs, K., Kääb, A., McMillan, M., McNabb, R., Nagler, T., Nuth, C., Rastner, P., Strozzi, T. and Wuite, J. (2017a): Error sources and guidelines for quality assessment of glacier area, elevation change, and velocity products derived from satellite data in the Glaciers_cci project. *Remote Sensing of Environment*, 203, 256-275.

Paul, F., Strozzi, T., Schellenberger, T. and Kääb, A. (2017b): The 2015 surge of Hispar Glacier in the Karakoram. Remote Sensing, 9(9), 888; doi: 10.3390/rs9090888.

Paul, F., Rastner, P., Azzoni, R.S., Diolaiuti, G., Fugazza, D., Le Bris, R., Nemec, J., Rabatel, A., Ramusovic, M., Schwaizer, G. and Smiraglia, C. (2020): Glacier shrinkage in the Alps continues unabated as revealed by a new glacier inventory from Sentinel-2. *Earth Systems Science Data*, 12(3), 1805-1821.

Peltier, W.R. (2004): Global glacial isostasy and the surface of the ice-age Earth: the ICE-5G (VM2) model and GRACE. *Annual Review of Earth and Planetary Sciences*, 32, 111-149.

Quincey, D.J., Glasser, N.F., Cook, S.J. and Luckman, A. (2015): Heterogeneity in Karakoram glacier surges. *Journal of Geophysical Research: Earth Surface*, 120(7), 1288–1300.

Rastner P., Strozzi, T. and Paul, F. (2017) : Fusion of multi-source satellite data and dems to create a new glacier inventory for Novaya Zemlya. *Remote Sensing*, 9(11):1122 ; doi: 10.3390/rs9111122.

Round, V., Leinss, S., Huss, M., Haemmig, C. and Hajnsek, I. (2017). Surge dynamics and lake outbursts of Kyagar Glacier, Karakoram. *The Cryosphere*, 11(2), 723–739.

Shean, D. 2017. *High Mountain Asia 8-meter DEM Mosaics Derived from Optical Imagery, Version 1*. Boulder, Colorado USA. NASA National Snow and Ice Data Center Distributed Active Archive Center; doi: https://doi.org/10.5067/KXOVQ9L172S2.

Shepherd, A., et al. (2019): Trends in Antarctic Ice Sheet elevation and mass. *Geophysical Research Letters*, 46 (14) 8174-8183.

Strozzi, T., Kääb, A. and Schellenberger, T. (2017a): Frontal destabilization of Stonebreen, Edgeøya, Svalbard. *The Cryosphere*, 11 (1), 553–566.

Strozzi T., Paul, F., Wiesmann, A., Schellenberger, T. and Kääb, A. (2017b): Circum-Arctic Changes in the Flow of Glaciers and Ice Caps from Satellite SAR Data between the 1990s and 2017. *Remote Sensing*, 9(9), 947 ; doi: 10.3390/rs9090947.

Strozzi T., Luckman, A., Murray, T., Wegmüller, U. and Werner, C. (2002) : Glacier motion estimation using SAR offset-tracking procedures. *IEEE Transactions on Geoscience and Remote Sensing*, 40, 2384-2391.

Strozzi T., Kouraev, A., Wiesmann, A., Wegmüller, U., Sharov, A. and Werner, C. (2008): Estimation of Arctic glacier motion with satellite L-band SAR data. *Remote Sensing of Environment*, 112, 636-645.

Tabachnick, B.G. and Fidell, L.S. (2019): Using Multivariate Statistics, seventh edition, published by Pearson, ISBN-13: 978-0-13-479054-1.

Treichler D. and Kääb A. (2016): ICESat laser altimetry over small mountain glaciers. *The Cryosphere*, 10, 2129-2146.

Ulaby, F.T., Moore, R.K. and Fung, A.K. (1982): M*icrowave remote sensing: active and passive*. Addison-Wesley Publishing Company, London [etc.].

Vaughan, D.G., Comiso, J.C., Allison, I., Carrasco, J., Kaser, G., Kwok, R. Mote, P., Murray, T., Paul, F., Ren, J., Rignot, E., Solomina, O., Steffen, K. and Zhang, T. (2013): *Observations: Cryosphere*. In: Climate Change 2013: The Physical Science Basis. Contribution of Working Group I to the Fifth Assessment Report of the IPCC. Cambridge University Press, Cambridge, United Kingdom and New York, NY, USA, pp. 317–382.

von Albedyll, L., H. Machguth, S.U. Nussbaumer and M. Zemp (2018). Elevation changes of Holm Land Ice Cap, northeast Greenland, from 1978 to 2012-2015 derived from high-

resolution digital elevation models. *Arctic, Antarctic and Alpine Research*, 50 (1), e1523638.

Wegmüller, U. and Werner, C. (1996): Land applications using ERS-1/2 tandem data. Proceedings of the Fringe 96 Workshop: ERS SAR Interferometry, Zurich, 30 September - 2 October 1996, ESA SP-406, 97–112.

Wegmüller U., Werner, C., Strozzi, T. and Wiesmann, A. (2006) : Ionospheric electron concentration effects on SAR and INSAR, Proceedings of IGARSS, Denver (USA), 31 July- 4 August 2006.

Wingham, D.J., Ridout, A.J., Scharroo, R., Arthern, R.J. and Shum, C.K (1998): Antarctic elevation change from 1992 to 1996. *Science*, 282, 456-458.

Winsvold H.S., Kääb A. and Nuth C. (2016): Regional glacier mapping using optical satellite data time series. *IEEE Journal of Selected Topics in Applied Earth Observations and Remote Sensing* 9(8), 3698-3711.

Yde, J.C. and Paasche, O. (2010): Reconstructing climate change: not all glaciers suitable. *EOS, Transactions American Geophysical Union* ,91(21), 189–190.

Zhou, Y., Li, Z. and Li, J. (2017): Slight glacier mass loss in the Karakoram region during the 1970s to 2000 revealed by KH-9 images and SRTM DEM. *Journal of Glaciology*, 63(238), 331–342.

Zhou, Y., Li, Z., Li, J., Zhao, R. and Ding, X. (2018): Glacier mass balance in the Qinghai–Tibet Plateau and its surroundings from the mid-1970s to 2000 based on Hexagon KH-9 and SRTM DEMs. *Remote Sensing of Environment*, 210, 96–112.

Contract: 4000127593/19/I-NB
Algorithm Theoretical Basis
Document (ATBD)

Name: Glaciers_cci+D2.1_ATBD
Version: 1.0
Date: 10.10.2020
Page: 46

6. Acronyms

ALOS	Advanced Land Observing Satellite
ASTER GDEM	Advanced Spaceborne Thermal Emission and Reflection Radiometer Global DEM
ATBD	Algorithm Theoretical Baseline Document
DEM	Digital Elevation Model
ERS	European Remote Sensing Satellite
ENVISAT	Environmental Satellite
ETM+	Enhanced Thematic Mapper plus
GCP	Ground Control Point
GEE	Google Earth Engine
HMA	High Mountain Asia
ICESat	Ice, Cloud, and land Elevation Satellite
InSAR	Interferometric SAR
IV	Ice Velocity
JERS	Japanese Earth Resource Satellite
LOS	Line Of Sight
MEaSUREs	Making Earth System Data Records for Use in Research Environments
NSIDC	National Snow and Ice Data Center
OT	Offset Tracking
PALSAR	Phased Array type L-band Synthetic Aperture Radar
RADAR	Radio Detection and Ranging
RGI	Randolph Glacier Inventory
RMSE	Root Mean Square Error
RSG	Remote Sensing software Graz
SAR	Synthetic Aperture Radar
SLC	Single Look Complex
SRTM	Shuttle Radar Topography Mission